universität wien

MASTERARBEIT | MASTER'S THESIS

Titel | Title

Machine learned molecular dynamics study of Jahn-Teller distortions in LaMnO3 and Ba2NaOsO6

verfasst von | submitted by

Alexander Ehrentraut BSc

angestrebter akademischer Grad | in partial fulfilment of the requirements for the degree of

Master of Science (MSc)

Wien | Vienna, 2025

Studienkennzahl lt. Studienblatt | Degree programme code as it appears on the student record sheet:	UA 066 876
Studienrichtung lt. Studienblatt | Degree programme as it appears on the student record sheet:	Masterstudium Physics
Betreut von | Supervisor:	Univ.-Prof. Dr.techn. Cesare Franchini

Abstract

The Jahn-Teller effect has been thoroughly investigated theoretically, experimentally and computationally during the last decades. One computational framework of choice in this field is density functional theory. A novel method that builds on density functional theory, the machine learned force field method [1, 2], has been employed successfully to predict the structural phase transition in $LaMnO_3$ [3], one of the principal materials that exhibit a cooperative Jahn-Teller effect. The present study builds upon this result by strengthening the evidence that the simulated transition is the experimentally observed [4, 5] structural phase transition. Further, the machine learned force field method is employed for Ba_2NaOsO_6. This material exhibits a magnetically and structurally ordered phase at low temperatures, which is succeded by a nematic phase upon heating until the material becomes cubic [6]. Strong spin-orbit coupling, interactions between structure and magnetism and the presence of a dynamic Jahn-Teller effect [7, 8] affect the application of the machine learned force field method to Ba_2NaOsO_6. The phase diagram is not sucessfully reproduced, while insights on the limitations of the machine learned force field method are provided.

Der Jahn-Teller-Effekt wurde in den letzten Jahrzehnten theoretisch, experimentell und mit computergestützten Methoden untersucht. Eines der wichtigsten Paradigmen in diesem Bereich ist die Dichtefunktionaltheorie. Eine neuartige Methode, die auf der Dichtefunktionaltheorie aufbaut, nämlich die Methode sogenannter *machine learned force fields* [1, 2], wurde erfolgreich eingesetzt, um den strukturellen Phasenübergang in $LaMnO_3$ vorherzusagen [3], einem der wichtigsten Materialien, die einen kooperativen Jahn-Teller-Effekt aufweisen. Die vorliegende Studie baut auf diesem Ergebnis auf, indem sie die Belege festigt, dass es sich bei dem simulierten Übergang um den experimentell beobachteten [4, 5] strukturellen Phasenübergang handelt. Darüber hinaus wird die Methode der machine learned force fields für Ba_2NaOsO_6 eingesetzt. Dieses Material weist bei niedrigen Temperaturen eine magnetisch und strukturell geordnete Phase auf, auf die bei Erwärmung eine nematische Phase folgt, bis das Material kubisch wird [6]. Eine starke Spin-Bahn-Kopplung, Wechselwirkungen zwischen Struktur und Magnetismus und das Vorhandensein eines dynamischen Jahn-Teller-Effekts [7, 8] beeinflussen die Anwendung der machine learned force fields Methode auf Ba_2NaOsO_6. Das Phasendiagramm kann nicht erfolgreich reproduziert werden, während Einblicke in die Grenzen der machine learned force fields gewonnen werden.

Acknowledgements

The computations for this study were conducted on the VSC-5 cluster of the Austrian Scientific Computing collaboration. The author thanks Univ. Prof. Cesare Franchini for supervising the development of the present thesis and Dr. Lorenzo Celiberti for valuable disussions throughout the entire process of working on this project. Further, the author is grateful for constant support and encouragement from his parents, whithout whom he would not have been able to study physics.

Contents

List of Figures

Introduction **i**

1 Physical background **1**
1.1 Crystal field 2
1.2 Spin-orbit coupling 6
1.3 Electron-phonon coupling 10
1.4 Jahn-Teller effect 13
1.4.1 Cooperative JTE and orbital ordering 17
1.4.2 Dynamic JTE 20

2 Computational methods **23**
2.1 Density functional theory 24
2.1.1 From the Thomas-Fermi model to the Kohn-Sham equations 24
2.1.2 Spin polarization and constrained noncollinear magnetic moments 30
2.1.3 Dudarev's +U correction 31
2.2 Molecular Dynamics 33
2.2.1 Velocity-Verlet algorithm 33
2.2.2 Langevin thermostat and the NpT ensemble 35
2.3 Machine learned force fields 36
2.3.1 On-the-fly training 36
2.3.2 Machine learning approach and descriptors 37

2.3.3 Error estimation with Bayesian linear regression 39

3 The perovskite $LaMnO_3$ **43**

4 The double perovskite Ba_2NaOsO_6 **47**
4.1 Physical properties of Ba_2NaOsO_6 48
4.2 The Jahn-Teller problem in Ba_2NaOsO_6 50

5 Results **53**
5.1 LMO 54
5.2 BNOO 63

6 Conclusions **71**

Appendix A: Formulae **75**

Appendix B: Octahedral rotations with the VanVleckCalculator **77**

Appendix C: LMO sample INCAR **79**

Appendix D: BNOO sample INCAR **83**

List of Figures

1.1 Shapes of electron densities related to (a, b) e_g and (c -e) t_{2g} wavefunctions. Figure taken from [10]. 4

1.2 Overlap of p-orbitals and $d_{x^2-x^2}$-orbital. Figure taken from [10]. 4

1.3 Contribution to crystal field splitting due to π-hybridization. a and b stand for (anti-)bonding, respectively. Figure taken from [10]. 6

1.4 Potential energy as a function of the distortion u. Figure taken from [10]. 15

1.5 "Mexican hat" potential energy surface of the coupling between the e_g states and (Q_3, Q_2) distortion modes. Figure taken from [10]. 16

1.6 Change of energy levels due to pseudo JTE. (a) Weak PJTE - the ground state is still stable. (b) Strong PJTE - the ground state bekomes unstable. Figure taken from [14]. 17

1.7 Shape of the field due to a JT-distorted ion. The light areas correspond to attraction and the dark areas to repulsion (or it is the other way round). Figure taken from [10]. 19

1.8 Adiabatic potential energy surface in the distortion coordinates for different strengths of spin-orbit coupling. q_{z^2} corresponds to Q_3 and $q_{x^2-y^2}$ to Q_2. The electronic ground states for the energetic minima of the distortion-modes are also indicated. (a) No spin-orbit-coupling. (b) Moderate spin-orbit coupling. (c) Strong spin-orbit coupling. The change of the adiabatic potential energy surface is due to the reduction of electron-phonon coupling by spin-orbit coupling [8]. Figure taken from [8]. 21

3.1 Structure of LMO in the orthorhombic Pbnm setting. Figure taken from [42]. 44

3.2 Orbital ordering in LMO. (a) Schematic representation with rotationally symmetric orbitals. (b) Closer to the real shape of the orbitals. The arrows indicate the direction of the Mn magnetic moments. Figure taken from [10]. 45

4.1 Unit cell of BNOO with 40 atoms. Figure taken from [**Cong**]. 48

4.2 Ground state magnetic ordering with connected JT-distortions in BNOO. Figure taken from [7]. 50

4.3 Numbering of the ligand oxygen ions for the definition of the Van Vleck normal coordinates. 52

5.1 LMO during T-ramp: averages of distortions of all octahedra in the supercell. Left: absolute value of Q_2-mode. Middle: Q_3-mode. Right: Magnitude of octahedral rotation. 55

5.2 LMO at $T = 100K$: a) averages of JT-modes Q_2 and Q_3 for each octahedron around an Mn-site. b) Pearson correlation coefficients of JT-modes for each site wrt. site with index 12. c) Heat map of occurrences of JT distortion values across time and entire supercell. Brighter colors indicate a higher probability of an octahedron having a given distortion. 55

5.3 LMO at $T = 600K$: a) averages of JT-modes Q_2 and Q_3 for each octahedron around an Mn-site. b) Pearson correlation coefficients of JT-modes for each site wrt. site with index 12. c) Heat map of occurrences of JT distortion values across time and entire supercell. Brighter colors indicate a higher probability of an octahedron having a given distortion. 56

5.4 LMO at $T = 900K$: a) averages of JT-modes Q_2 and Q_3 for each octahedron around an Mn-site. b) Pearson correlation coefficients of JT-modes for each site wrt. site with index 12. c) Heat map of occurrences of JT distortion values across time and entire supercell. Brighter colors indicate a higher probability of an octahedron having a given distortion. 56

5.5 Distribution of Q2 mode in LMO for different temperatures. . 57

5.6 LMO at $T = 100K$: a) averages of JT-modes Q_4, Q_5 and Q_6 for each octahedron around an Mn-site. b) Pearson correlation coefficients of JT-modes for each site wrt. site with index 12. c) Heat map of occurrences of JT distortion values across time and entire supercell. Brighter colors indicate a higher probability of an octahedron having a given distortion. 58

5.7 LMO at $T = 600K$: a) averages of JT-modes Q_4, Q_5 and Q_6 for each octahedron around an Mn-site. b) Pearson correlation coefficients of JT-modes for each site wrt. site with index 12. c) Heat map of occurrences of JT distortion values across time and entire supercell. Brighter colors indicate a higher probability of an octahedron having a given distortion. 59

5.8 LMO at $T = 900K$: a) averages of JT-modes Q_4, Q_5 and Q_6 for each octahedron around an Mn-site. b) Pearson correlation coefficients of JT-modes for each site wrt. site with index 12. c) Heat map of occurrences of JT distortion values across time and entire supercell. Brighter colors indicate a higher probability of an octahedron having a given distortion. 60

5.9 LMO: Velocity-autocorrelation times of all Van Vleck modes and octahedral rotations as functions of temperature. The dashed lines are only guides for the eyes. 60

5.10 LMO: Velocity-autocorrelation functions of Q2 and Q3 for indices 0 and 27 for: top row: T = 100K; middle row: T= 600K; bottom row: T = 900K. x-axis: t [ps] 61

5.11 LMO: Velocity-autocorrelation times of La DOF as functions of temperature. The dashed lines are only guides for the eyes. 61

5.12 LMO: Velocity-autocorrelation functions of DOF of one La-ion for: top row: T = 100K; middle row: T= 600K; bottom row: T = 900K. x-axis: t [ps] 62

5.13 BNOO at $T = 1K$: a) averages of JT-modes Q_2 and Q_3 for each octahedron around an Os-site. b) Pearson correlation coefficients of JT-modes for each site wrt. site with index 12. c) Heat map of occurrences of JT distortion values across time and entire supercell. Brighter colors indicate a higher probability of an octahedron having a given distortion. 64

5.14 BNOO at $T = 1K$: a) averages of JT-modes Q_4, Q_5 and Q_6 for each octahedron around an Os-site. b) Pearson correlation coefficients of JT-modes for each site wrt. site with index 12. c) Heat map of occurrences of JT distortion values across time and entire supercell. Brighter colors indicate a higher probability of an octahedron having a given distortion. 65

5.15 BNOO at $T = 1K$: a) averages of components of rotation vector for each octahedron around an Os-site. b) Pearson correlation coefficients of components of rotation vectors for each site wrt. site with index 12. c) Heat map of occurrences of rotation vector components across time and entire supercell. Brighter colors indicate a higher probability of an octahedron having a given rotation. 66

5.16 Time series for rotation vector components of octahedron with index 1 for T = a) 1K, b) 15K, c) 20K, d) 25K, e) 40K. 67

5.17 BNOO: Velocity-autocorrelation functions of Q2 and Q3 for indices 0 and 27 for: top row: T = 1K; middle row: T= 20K; bottom row: T = 40K. x-axis: t [ps] 68

5.18 BNOO: Velocity-autocorrelation times of all Van Vleck modes and octahedral rotations as functions of temperature. The dashed lines are only guides for the eyes. 68
5.19 LMO: Velocity-autocorrelation functions of DOF of one Ba-ion for: top row: T = 1K; middle row: T= 20K; bottom row: T = 40K. x-axis: t [ps] 69
5.20 BNOO: Velocity-autocorrelation times of Ba DOF as functions of temperature. The dashed lines are only guides for the eyes. 70

Introduction

The Jahn-Teller effect is a well understood phenomenon that describes the fact that degeneracies in the electronic ground state of a system are lifted by structural distortions due to electron-phonon coupling. [9, 10]. This theorem that was proven from group theoretical considerations has physical consequences, namely structural distortions, for a multitude of materials. One of the principal crystal structures for which this effect plays a role is the perovskite structure and in this class, lanthanum manganite ($LaMnO_3$, LMO) is known as the prime example of a material that exhibits a strong Jahn-Teller effect. However, the structural distortions, which are cooperatively ordered and give rise to a metrically orthorhombic lattice, only occur under a certain temperature threshold. Above the phase transition, the lattice is metrically cubic. To the knowledge of the authors of the present study, this phase transition has been simulated with the use of molecular dynamics for the first time in 2023 [3]. To this end, the authors of the mentioned study used a novel method that incorporates machine learning (so called machine learned force fields, MLFF) to retain the accuracy of density functional theory calculations for molecular dynamics simulations on larger time scales and for larger systems without introducing unreasonably high computation times. These methods are explained below. The first aim of the present study is to reproduce the findings of this first successful investigation of a Jahn-Teller phase transition with MLFF and to build upon it. The method shall then be applied to a second material.

Ba_2NaOsO_6 (BNOO) is a crystal with double perovskite structure that exhibits a wide range of physical phenomena that interact with each other.

Structurally, it transitions from a cubic symmetry to a phase with so called broken local point symmetry at low temperatures, before exhibiting cooperatively ordered distortions at even lower temperatures [11]. It also has an exotic magnetic ground state of non-collinear magnetic moments that are ordered close to an antiferromagnetic ordering, but canted [7, 6]. Furthermore, the magnetic ground state is strongly influenced by the structure [7]. In addition to these effects, electronic correlation, which makes BNOO a Mott insulator, and spin-orbit coupling, which arises from a relativistic treatment of the electrons, have an impact on the physical properties of this material [12, 11]. BNOO has also been reported to exhibit a dynamic Jahn-Teller effect which arises from the quantum mechanical treatment of Jahn-Teller distortions and influences its structural, electronic and magnetic properties [8, 13]. The second aim of this study is to apply the MLFF method to BNOO to investigate whether fingerprints of the above described phenomena can be captured in molecular dynamics simulation and to potentially open the door to further insights into the physics of this peculiar material using the MLFF method.

Chapter 1

Physical background

The Jahn-Teller effect is one of the most studied phenomena in solid state physics and also led to the discovery of high T_c superconductivity and colossal magnetoresistance [14]. The development of the relevant theory started in 1937 when Hermann Arthur Jahn and Edward Teller published a mathematical proof of the fact that electronic degeneracies in molecular systems generally lead to structural instabilities [9]. To understand various forms of the Jahn-Teller effect, from the case of an isolated Jahn-Teller active ion in a crystal to cooperative and dynamic JTE, multiple ingredients that go beyond band theory are necessary, as is often the case in solid state physics. This chapter will therefore first deal with crystal field splitting, spin-orbit coupling and electron-phonon coupling before introducing the Jahn-Teller effect. Knowledge of band theory, the Hubbard model that describes Mott insulators [10] and the non-relativistic description of hydrogen-like atoms, as well as quantum mechanical formalism (including second quantization) and basic crystallography is assumed. It should further be noted that this chapter is intended as a brief overview of the physics relevant to this study, not as a rigorous derivation of all the theory. To this end, whole chapters and even books on the presented topics have been written.

1.1 Crystal field

This section deals with the effect of crystal field splitting. It follows the explanation given in Chapter 3.1 in *Transition Metal Compounds* by Daniel I. Khomskii [10].

In an isolated spherically symmetric transition metal ion, the d levels ($l = 2, l^z = -2, -1, 0, 1, 2$) are fivefold degenerate. Introducing such an ion into a crystal, the new local point symmetry, which is determined by the crystal lattice, can lead to a splitting of this degeneracy (crystal field splitting). This is due to the interaction of the transition metal electrons with the surrounding ions, and the type of the resulting splitting depends on the local symmetry. For example, if a transition metal ion is surrounded by six ligand anions (e.g. O^{2-}) in the shape of an octahedron (such as is the case in perovskites), group theoretical arguments show that the d levels are split into a lower triplet (called t_{2g}) and a higher doublet (called e_g). These wavefunctions can be explicitly written down using real combinations of the spherical harmonics $|l^z\rangle := |l = 2, l^z\rangle$:

$$e_g : \begin{cases} |z^2\rangle = |3z^2 - r^2\rangle = |l^z = 0\rangle \sim \frac{1}{2}(3z^2 - r^2) = \frac{1}{2}(2z^2 - x^2 - y^2), \\ |x^2 - y^2\rangle = \frac{1}{\sqrt{2}}(|2\rangle + |-2\rangle) \sim \frac{\sqrt{3}}{2}(x^2 - y^2), \end{cases} \tag{1.1}$$

$$t_{2g} : \begin{cases} |xy\rangle = \frac{-i}{\sqrt{2}}(|2\rangle - |-2\rangle) \sim \sqrt{3}xy, \\ |xz\rangle = \frac{-1}{\sqrt{2}}(|1\rangle - |-1\rangle) \sim \sqrt{3}xz, \\ |yz\rangle = \frac{i}{\sqrt{2}}(|1\rangle + |-1\rangle) \sim \sqrt{3}yz. \end{cases} \tag{1.2}$$

The reason for the splitting of energy levels is now twofold. One contribution is due to Coulomb repulsion of point charge distributions, which is easily understood qualitatively by looking at the shapes of the charge distributions connected to the wavefunctions in (1.1) and (1.2), which are shown

in Fig. 1.1. The lobes of the orbitals corresponding to the e_g levels point directly in the directions of the ligands, which are anions. Thus, their negative electron charge densitiy experiences strong Coulomb repulsion, leading to an increase in energy. The lobes of the t_{2g} orbitals, however, point in the directions between the ligands and, therefore, experience less Coulomb repulsion. As a consequence, the e_g levels are higher in energy than the t_{2g} levels.

The second contribution to crystal field splitting comes from covalency. To understand this, the case where O^{2-} anions form the ligands is explained below. Consider again the lobes of the e_g orbitals. They have significant overlap with the lobes of those 2p orbitals of the oxygen anions that point in the direction of the TM-O bond as shown in Fig. 1.2.

This overlap opens up the possibility of hopping between orbitals with hopping matrix elements (here for hopping between the $d_{x^2-y^2}$ orbital and the $2p_x$ orbitals of O1 and O3 as well as the $2p_y$ orbitals of O2 and O4):

$$\mathcal{H}_{pd} = t_{pd\sigma}[d^\dagger_{x^2-y^2}(p_{1x} + p_{2y} + p_{3x} + p_{4y}) + h.c.]. \tag{1.3}$$

$d^\dagger, p^\dagger, d, p$ are the creation and annihilation operators of electrons in the respective orbitals. This type of hybridization, called σ-hybridization, leads to a Hamiltonian with matrix:

$$\begin{pmatrix} \epsilon_d & t_{pd\sigma} \\ t_{pd\sigma} & \epsilon_p \end{pmatrix} \tag{1.4}$$

with respect to the basis of d and p states. Its eigenvalues are:

$$\epsilon_{a,b} = \frac{\epsilon_d + \epsilon_p}{2} \pm \sqrt{\frac{(\epsilon_d - \epsilon_p)^2}{4} + t^2_{pd\sigma}}, \tag{1.5}$$

which, for $t_{pd\sigma} \ll \epsilon_d - \epsilon_p$, becomes:

$$\begin{aligned} \epsilon_a &= \epsilon_d + \frac{t^2_{pd\sigma}}{\epsilon_d - \epsilon_p}, \\ \epsilon_b &= \epsilon_p - \frac{t^2_{pd\sigma}}{\epsilon_d - \epsilon_p}. \end{aligned} \tag{1.6}$$

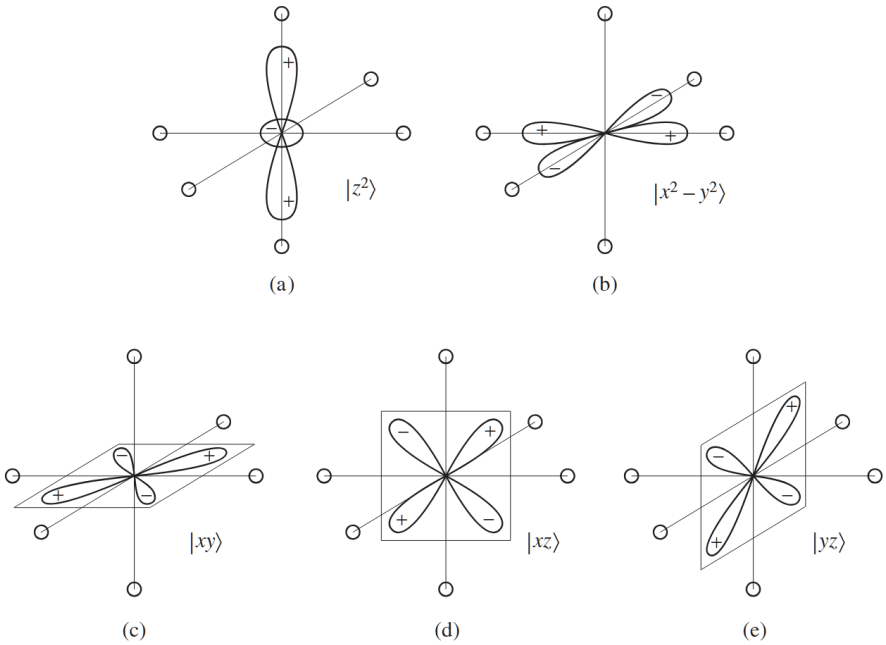

Figure 1.1: Shapes of electron densities related to (a, b) e_g and (c -e) t_{2g} wavefunctions. Figure taken from [10].

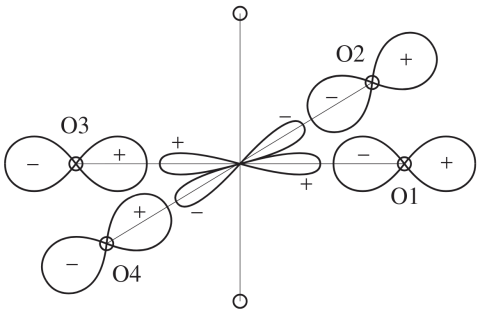

Figure 1.2: Overlap of p-orbitals and $d_{x^2-x^2}$-orbital. Figure taken from [10].

The subscripts a and b stand for antibonding and bonding, respectively. This leads to antibonding and bonding eigenstates:

$$\begin{aligned} |\psi_a\rangle &= \beta\,|p\rangle - \alpha\,|d\rangle\,, \\ |\psi_b\rangle &= \alpha\,|p\rangle + \beta\,|d\rangle\,, \end{aligned} \tag{1.7}$$

with $\alpha \gg \beta$. The energy difference between bonding and antibonding states is smaller for the t_{2g} levels than for the e_g levels. This is because the t_{2g} orbitals do not overlap with the p orbitals in the direction of the TM-O bond, but those perpendicular to it (π-hybridization), and this is weaker than σ-hybridization. From this follows that the antibonding t_{2g} states are lower in energy than the antibonding e_g states, yielding the same type of splitting as the point charge contribution, which can be seen in Fig. 1.3. The bonding states are typically filled and, therefore, are not of interest for crystal field splitting.

Breaking of the cubic point symmetry can lead to further splitting. For example, when the ligand octahedron is tetragonally elongated along the z-axis, the degeneracy of the e_g levels is lifted. This is because the Coulomb repulsion of the $|z^2\rangle$ states and the overlap of the $|z^2\rangle$ orbital with the $2p_z$ orbitals decrease. The opposite is true for the $|x^2 - y^2\rangle$ states. As a result, the $|z^2\rangle$ level is lowered and the $|x^2 - y^2\rangle$ level is elevated.

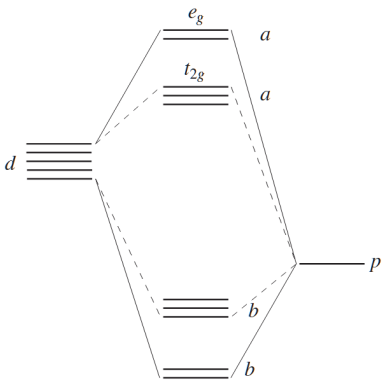

Figure 1.3: Contribution to crystal field splitting due to π-hybridization. a and b stand for (anti-)bonding, respectively. Figure taken from [10].

1.2 Spin-orbit coupling

Spin-orbit coupling is a phenomenon in atomic physics that arises from the relativistic description of the electrons. It shall now be explained using the Dirac equation as a starting point and following the description in Appendix 7 of *Physics of Atoms and Molecules* by B. Brandsen and C. Joachain [15]. The Dirac equation for a particle with spin 1/2 in an electromagnetic field $(\mathbf{A}, \phi)$ reads:

$$i\hbar\frac{\partial\mathbf{\Psi}}{\partial t} = \left[c\boldsymbol{\alpha}(\mathbf{p} - q\mathbf{A}) + q\phi + \beta mc^2\right]\mathbf{\Psi}, \tag{1.8}$$

where in the non-relativistic limit $\boldsymbol{\alpha}$ and β can be taken as 4x4-matrices:

$$\begin{aligned}\alpha_i &= \begin{pmatrix} 0 & \sigma_i \\ \sigma_i & 0 \end{pmatrix}, \\ \beta &= \begin{pmatrix} \mathbb{I} & 0 \\ 0 & -\mathbb{I} \end{pmatrix},\end{aligned} \tag{1.9}$$

with σ_i being the pauli matrices. $\mathbf{\Psi}$ is a four-component spinor of a spin 1/2 particle and its antiparticle. Looking at stationary solutions $\mathbf{\Psi} = \boldsymbol{\chi}(\mathbf{r})e^{-iEt/\hbar}$, with:

$$\boldsymbol{\chi}(\mathbf{r}) = \begin{pmatrix} \boldsymbol{\psi}(\mathbf{r}) \\ \boldsymbol{\eta}(\mathbf{r}) \end{pmatrix}, \tag{1.10}$$

one has two coupled equations:

$$\begin{aligned} E\boldsymbol{\psi}(\mathbf{r}) - c\boldsymbol{\sigma}(\mathbf{p} - q\mathbf{A})\boldsymbol{\eta}(\mathbf{r}) - (q\phi + mc^2)\boldsymbol{\psi}(\mathbf{r}) = 0, \\ E\boldsymbol{\eta}(\mathbf{r}) - c\boldsymbol{\sigma}(\mathbf{p} - q\mathbf{A})\boldsymbol{\psi}(\mathbf{r}) - (q\phi - mc^2)\boldsymbol{\eta}(\mathbf{r}) = 0. \end{aligned} \tag{1.11}$$

For atoms, it is reasonable to assume $\mathbf{A} = 0$ and $q\phi = V(r)$. Further, writing $E = E' + mc^2$ (1.11) becomes:

$$\begin{aligned} E'\boldsymbol{\psi}(\mathbf{r}) - c(\boldsymbol{\sigma}\mathbf{p})\boldsymbol{\eta}(\mathbf{r}) - V(r)\boldsymbol{\psi}(\mathbf{r}) = 0, \\ (E' - 2mc^2)\boldsymbol{\eta}(\mathbf{r}) - c(\boldsymbol{\sigma}\mathbf{p})\boldsymbol{\psi}(\mathbf{r}) - V(r)\boldsymbol{\eta}(\mathbf{r}) = 0. \end{aligned} \tag{1.12}$$

$\boldsymbol{\eta}(\mathbf{r})$ is then:

$$\boldsymbol{\eta}(\mathbf{r}) = \frac{c(\boldsymbol{\sigma}\mathbf{p})\boldsymbol{\psi}(\mathbf{r})}{E' - 2mc^2 - V(r)}, \tag{1.13}$$

and one obtains the following equation for $\boldsymbol{\psi}(\mathbf{r})$ (with $\mathbf{p} = -i\hbar\boldsymbol{\nabla}$):

$$E'\boldsymbol{\psi}(\mathbf{r}) = -c^2\hbar^2(\boldsymbol{\sigma}\boldsymbol{\nabla})\frac{1}{E' - 2mc^2 - V(r)}(\boldsymbol{\sigma}\boldsymbol{\nabla})\boldsymbol{\psi}(\mathbf{r}) + V(r)\boldsymbol{\psi}(\mathbf{r}). \tag{1.14}$$

Using the approximation:

$$\frac{1}{E' - 2mc^2 - V(r)} \approx \frac{1}{2mc^2}\left(1 - \frac{E' - V(r)}{2mc^2}\right), \tag{1.15}$$

the Schrödinger equation for $\boldsymbol{\psi}(\mathbf{r})$ becomes:

$$\begin{aligned} E'\boldsymbol{\psi}(\mathbf{r}) = &- \frac{\hbar^2}{2m}\left(1 - \frac{E' - V(r)}{2mc^2}\right)(\boldsymbol{\sigma}\boldsymbol{\nabla})^2\boldsymbol{\psi}(\mathbf{r}) \\ &- \frac{\hbar^2}{4m^2c^2}(\boldsymbol{\sigma}\boldsymbol{\nabla}V(r))(\boldsymbol{\sigma}\boldsymbol{\nabla}\boldsymbol{\psi}(\mathbf{r})) + V(r)\boldsymbol{\psi}(\mathbf{r}). \end{aligned} \tag{1.16}$$

After some nontrivial steps, this becomes:

$$E'\boldsymbol{\psi}(\mathbf{r}) = \left[\frac{p^2}{2m} + V(r) + \frac{p^4}{8m^3c^2} + \frac{1}{2m^2c^2r}\frac{dV}{dr}\mathbf{LS} + \frac{\hbar^2}{8m^2c^2}\boldsymbol{\nabla}^2V(r)\right]\boldsymbol{\psi}(\mathbf{r}), \tag{1.17}$$

where one has three corrections to the non-relativistic description of an electron in a spherical potential.

$$\frac{p^4}{8m^3c^2} \tag{1.18}$$

is the first order relativistic correction to the kinetic energy,

$$\frac{1}{2m^2c^2r}\frac{dV}{dr}\mathbf{LS} \tag{1.19}$$

is the spin-orbit coupling term with angular momentum operator $\mathbf{L}$ and spin operator $\mathbf{S}$ and

$$\frac{\hbar^2}{8m^2c^2}\boldsymbol{\nabla}^2 V(r) \tag{1.20}$$

is the Darwin term. The spin-orbit coupling term makes commutators $[\mathcal{H}, \mathbf{L}]$ and $[\mathcal{H}, \mathbf{S}]$ nonzero and the state of a one-electron atom is therefore not described by the set of quantum numbers (n, l, m_l, m_s). Instead, a complete set of commuting observables is given by (n, l, j, m_j), with

$$\begin{aligned} j &= l \pm 1/2 \quad l \neq 0 \\ j &= 1/2 \qquad\quad l = 0 \end{aligned} \tag{1.21}$$

and

$$m_j = -j, -j+1, \ldots, j, \tag{1.22}$$

where the energy levels are split by the m_j, as described in Chapter 5 of [15].

The reference for the following description of the multi-electron case is taken from Chapter 2 of [10]. The spin-orbit correction becomes:

$$\mathcal{H}_{SO} = \sum_i \xi_i \mathbf{l}_i \mathbf{S}_i, \tag{1.23}$$

where the sum goes over all the electrons and the $\mathbf{l}_i$ are the angular momentum operators for individual electrons. There are now two limiting cases to construct the total angular momentum of all the electrons depending on the strength of the spin-orbit interaction. One could either first calculate the total angular momentum of individual electrons ($\mathbf{j}_i = \mathbf{l}_i + \mathbf{s}_i$) and then sum over all electrons:

$$\mathbf{J} = \sum_i \mathbf{j}_i. \tag{1.24}$$

This coupling provides the correct results for spin-orbit coupling that is stronger than the electron-electron interactions and is called *jj-coupling*. If the spin-orbit interaction is weak, however, one first calculates the total angular momentum and spin of all electrons:

$$\mathbf{L} = \sum_i \mathbf{l}_i \quad \mathbf{S} = \sum_i \mathbf{S}_i, \tag{1.25}$$

which then add to the total angular momentum:

$$\mathbf{J} = \mathbf{L} + \mathbf{S}. \tag{1.26}$$

This is called *LS-coupling* or *Russell-Saunders-coupling*. The total spin-orbit Hamiltonian then becomes:

$$\mathcal{H}_{SO} = \lambda \mathbf{LS}, \tag{1.27}$$

where, for one partially filled shell:

$$\lambda = \pm \frac{\xi}{2S}. \tag{1.28}$$

λ is positive for less-than-half filled shells and negative for more-than-half filled shells. The expectation of **LS** is given by:

$$\langle \mathbf{LS} \rangle = \frac{J(J+1) - L(L+1) - S(S+1)}{2}, \tag{1.29}$$

where J, L and S are quantum numbers for total angular momentum, total orbital moment and total spin. According to quantum mechanical rules for adding angular momenta, J can take the following values:

$$J = L + S, L + S - 1, \ldots, |L - S|. \tag{1.30}$$

From this it can be seen that energy levels increase with J for less-than-half filled shells (normal multiplet structure), but decrease with J for more-than-half filled shells (inverted multiplet structure). LS-coupling captures the situation well for 3d-ions, while jj-coupling is accurate for 4f- and 5f-ions. For 4d- and 5d-ions, an intermediate description might be required.

Spin orbit coupling shall now be applied to d states affected by a crystal field (see Chapter 3.1 of [10]). The t_{2g} states in (1.2) can also be expressed in the basis:

$$\begin{aligned} |t_{2g}^{0}\rangle &= -\frac{i}{\sqrt{2}}(|2\rangle - |-2\rangle) = |xy\rangle\,, \\ |t_{2g}^{1}\rangle &= |1\rangle \sim -\frac{1}{\sqrt{2}}(|xz\rangle + i\,|yz\rangle), \\ |t_{2g}^{-1}\rangle &= |-1\rangle \sim \frac{1}{\sqrt{2}}(|xz\rangle - i\,|yz\rangle)\,, \end{aligned} \tag{1.31}$$

from which it can be seen that this triplet can be assigned an effective orbital momentum $\tilde{l} = 1$ with $l_z = 0, \pm 1$. This effective orbital momentum couples to the electrons' spin magnetic moments, leading to spin-orbit coupling like in an isolated atom ($\tilde{J} = |\tilde{l} - S|, ..., \tilde{l} + S$). The only difference is that it can be shown that the coupling constant $\tilde{\lambda}$ and the effective gyromagnetic ratio $\tilde{g}$ are negative. For this reason, the energy ordering of the different multiplet levels is exactly reversed with respect to the isolated transition metal atom: For shells with less than half of the maximum occupation, the multiplet levels with higher degeneracy (higher $\tilde{J}$) are lower, while the levels with lower $\tilde{J}$ are lower in energy for more-than-half filled shells.

1.3 Electron-phonon coupling

Now, the concept of electron-phonon coupling that constitutes a correction to the adiabatic approximation for the total wavefunction of a molecule or crystal shall be explained. First, it is described how one can go about including non-adiabatic corrections to the total wavefunction of a system. The second part of this section is concerned with electron-phonon interactions in the language of second quantization.

The central feature of various forms of the adiabatic approximation is the separation of the total wavefunction of a system into a mere product of an electronic and an ionic wavefunction [16]:

$$\Psi_{jt}(\mathbf{r}, \mathbf{Q}) = \psi_j(\mathbf{r}, \mathbf{Q})\chi_{jt}(\mathbf{Q}). \tag{1.32}$$

This is an approximation because the total Hamiltonian of the system

$$\mathcal{H} = T_e(\mathbf{r}) + T_n(\mathbf{Q}) + U(\mathbf{r}, \mathbf{Q}) + V(\mathbf{Q}), \tag{1.33}$$

where T_e and T_n are the kinetic energies of the electrons and nuclei, V is the potential energy of the nuclei and U is the Coulomb energy between electrons and electrons as well as electrons and nuclei, does generally not allow for a separation of variables. The justification for the adiabatic approximation is that the nuclei can be approximated to be static on the time scale of electronic motion.

Solving the Schrödinger equation for the Hamiltonian only depending on electronic degrees of freedom:

$$\mathcal{H}_{elec} = T_e(\mathbf{r}) + U(\mathbf{r}, \mathbf{Q}), \tag{1.34}$$

one obtains a set of wavefunctions $\psi_i(\mathbf{r}, \mathbf{Q})$ that is a complete basis for the electronic coordinates $\mathbf{r}$ [16]. One can therefore construct the total wavefunction as a series expansion in $\{\psi_i\}$ [16]:

$$\Psi_t(\mathbf{r}, \mathbf{Q}) = \sum_i \psi_i(\mathbf{r}, \mathbf{Q})\chi_{it}(\mathbf{Q}). \tag{1.35}$$

One can obtain the Ψ_t by plugging the series expansion into (1.33) and integrating over electronic coordinates, yielding a system of coupled differential equations for the χ_{it} [16]. However this approach does not seem feasible for large systems [16]. Another approach is to approximate the total wavefunction Ψ as a linear combination of adiabatic solutions [16]:

$$\Psi_{it} = \Psi_{it}^{AD} + \sum_{it \neq kr} C_{it,kr}\Psi_{kr}^{AD}. \tag{1.36}$$

Here, the Ψ^{AD} take the form of (1.32). The mixing matrix elements are obtained in first order perturbation theory via [16]:

$$C_{ir,kr} = \frac{\langle \psi_{kr}^{AD} | \, \mathcal{H} \, | \psi_{it}^{AD} \rangle - E_{kr}^{AD} \langle \psi_{kr}^{AD} | \psi_{it}^{AD} \rangle}{E_{it}^{AD} - E_{kr}^{AD}}. \tag{1.37}$$

It should be noted that this approach is not valid if the Ψ^{AD} are degenerate. Nevertheless, one can compute the secular determinant and solve the problem this way [16].

Now, the interaction between electrons and phonons in second quantization shall be described. The Born-Oppenheimer approximation, a particular form of the adiabatic approximation [16], describes the electron-lattice system to the lowest order in $\kappa = (m/M)^{1/4}$, where m and M are the electronic and ionic masses [17]. Including the next higher order of κ leads to a non diagonal matrix element in the electronic Hamiltonian $\mathcal{H}_{elec}$ [17]:

$$\langle \psi_i | \, \delta_{\mathbf{Q}} U \, | \psi_j \rangle \, , \tag{1.38}$$

where $\mathbf{Q} = \mathbf{Q_0} + \mathbf{u}$ and $\mathbf{u}$ is a displacement of the lattice configuration from its ground state $\mathbf{Q_0}$ [17]. In a solid, it takes the form:

$$\delta_{\mathbf{Q}} U = \mathbf{u}\, \epsilon^{-1} \nabla U|_{\mathbf{Q_0}}, \tag{1.39}$$

where ϵ^{-1} is the inverse of the dielectric matrix [17]. In second quantization, such interactions, which allow for transitions between different electronic eigenstates, can be described by an absorption or emission of phonons, which are quantized excitations of the crystal lattice vibrations. The Hamiltonian can be written as [17]:

$$\mathcal{H} = \mathcal{H}_e + \mathcal{H}_{ph} + \mathcal{H}_{e-ph}. \tag{1.40}$$

$\mathcal{H}_e$ describes the energy of the electrons modeled as non-interacting quasi-particles in stationary band-eigenstates in a periodic lattice [17]:

$$\mathcal{H}_e = \sum_{\mathbf{k}\nu\sigma} \epsilon_{\mathbf{k}\nu} c^\dagger_{\mathbf{k}\nu\sigma} c_{\mathbf{k}\nu\sigma}, \tag{1.41}$$

where $\epsilon_{\mathbf{k}\nu}$ is the energy of an electron with band index ν and momentum $\mathbf{k}$ and $c^\dagger_{\mathbf{k}\nu\sigma}, c_{\mathbf{k}\nu\sigma}$ are the creation and annihilation operators with a specific band index, momentum and spin σ. The product of creation and annihilation operator is the number operator with eigenvalues zero and one, since electrons are fermions. Similarly, the phonon Hamiltonian is [17]:

$$\mathcal{H}_{ph} = \sum_{\mathbf{q}j} \omega_{\mathbf{q}j} \left(b^\dagger_{\mathbf{q}j} b_{\mathbf{q}j} + \frac{1}{2} \right), \tag{1.42}$$

where $\omega_{\mathbf{q}j}$ is the energy (or rather frequency, but in natural units $\hbar = 1$) of a phonon with momentum $\mathbf{q}$ and branch index j. $b^\dagger_{\mathbf{q}j}, b_{\mathbf{q}j}$ are the phonon creation and annihilation operators. Notice how $\mathcal{H}_{ph}$ resembles the harmonic oscillator Hamiltonian. $\mathcal{H}_{e-ph}$ describes the interactions of electrons and phonons in the lowest order [17]:

$$\mathcal{H}_{e-ph} = \sum_{\mathbf{k}\nu\nu'\sigma} \sum_{\mathbf{q}j} g^{\mathbf{q}j}_{\mathbf{k}+\mathbf{q}\nu',\mathbf{k}\nu} c^\dagger_{\mathbf{k}+\mathbf{q}\nu'\sigma} c_{\mathbf{k}\nu\sigma} \left(b_{\mathbf{q}j} + b^\dagger_{-\mathbf{q}j} \right). \tag{1.43}$$

The term inside the sum describes the transition of an electron from a state $|\mathbf{k}, \nu\rangle$ to a state $|\mathbf{k}+\mathbf{q}, \nu'\rangle$ by either absorbing a phonon with momentum $\mathbf{q}$

or emission a phonon with momentum $-\mathbf{q}$ [17]. The matrix elements g that measure the probability of such an event are given by [17]:

$$g^{\mathbf{q}j}_{\mathbf{k}+\mathbf{q}\nu',\mathbf{k}\nu} = \sum_{s\alpha} A^{\mathbf{q}j}_{s\alpha} \langle \mathbf{k}+\mathbf{q}, \nu'\sigma | \delta^{\mathbf{q}}_{s\alpha} U | \mathbf{k}, \nu\sigma \rangle \,. \tag{1.44}$$

s is the index for a specific atom in the unit cell, α are cartesian indices, $\delta^{\mathbf{q}}_{s\alpha}U$ is the displacement of atom s in direction α due to phonon modes with momentum $\mathbf{q}$. The coefficients A are [17]:

$$A^{\mathbf{q}j}_{s\alpha} = \frac{\eta_{s\alpha}(\mathbf{q}j)}{\sqrt{2M_s\omega_{\mathbf{q}j}}}, \tag{1.45}$$

where $\eta_{s\alpha}(\mathbf{q}j)$ is the eigenvector of the mode $\mathbf{q}j$ and M_s is the mass of atom s. The Jahn-Teller effect, which is described in the next section, can only occur if there are sufficiently large non-diagonal elements with respect to band index in equation (1.44). This is the case for degenerate or nearly degenerate bands because only then there is significant overlap of electronic states.

The concept of electron-phonon coupling is important for understanding the Jahn-Teller effect, described in section 1.4. The cooperative Jahn-Teller effect can be understood within a semiclassical approach. Nevertheless, its fully quantum mechanical description and the dynamic Jahn-Teller effect require electron-phonon coupling.

1.4 Jahn-Teller effect

This section treats first the Jahn-Teller effect for an isolated Jahn-Teller ion in a crystal according to Chapter 3.2 in [10]. Then, the cooperative Jahn-Teller effect (CJTE) and the related phenomenon of orbital ordering is described. Finally, the dynamic Jahn-Teller effect and the conditions under which it arises are explained.

At the end of section 1.1, it has been described how the reduction of the local symmetry around a transition metal ion can further split the d levels. The tetragonal elongation of the octahedron along the z-axis has been used

as an example. Note that a tetragonal compression would lead to an inverted splitting of e_g levels. There is an important theorem from group theory that comes into play in such cases: *"All non-linear nuclear configurations are [...] unstable for an orbitally degenerate electronic state."* [9] This instability leads to a distortion of the crystal around an ion with orbital degeneracy. In general, the splitting of energy levels is most often linear in the corresponding distortion. If g is the coupling constant between electrons and lattice an u is the magnitude of the distortion, then the e_g levels are shifted by $\pm$gu. This can be added as a correction to the harmonic approximation, yielding:

$$E(u) = \pm gu + \frac{1}{2}Bu^2. \tag{1.46}$$

As can be seen from above, a tetragonal elongation is connected to the occupation of the $|z^2\rangle$ orbital, while a compression is connected to an occupied $|x^2 - y^2\rangle$ orbital Fig. 1.4 shows the energy as a function of the distortion u.

The energy gain is then

$$E_{JT} = \frac{g^2}{2B} \tag{1.47}$$

and the distortion u that minimizes the energy is

$$u_0 = \pm\frac{g}{B}. \tag{1.48}$$

In addition to tetragonal distortions, which shall henceforth be denoted by $Q_3 := \frac{1}{\sqrt{6}}(2\delta z - \delta x - \delta y)$, orthorhombic distortions, denoted by $Q_2 := \frac{1}{\sqrt{2}}(\delta x - \delta y)$, also split the e_g levels. The δx, δy, δz are the displacements of the ligand atoms from their high symmetry positions. The distortion modes Q_2 and Q_3 also split the t_{2g} levels.

Now it can be easily seen that, due to symmetry, not only a Q_3-distortion along the z-direction would lower the energy of the system, but also along the x- and y- directions. These distortions correspond to wavefunctions $|x^2\rangle$, $|y^2 - z^2\rangle$ and $|y^2\rangle$, $|x^2 - z^2\rangle$ respectively, which can be constructed as superpositions of $|z^2\rangle$ and $|x^2 - y^2\rangle$. The distortions themselves are linear combinations of Q_2 and Q_3 (a tetragonal mode in x-direction would be written

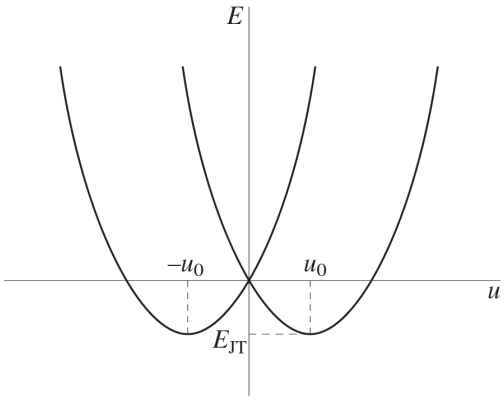

Figure 1.4: Potential energy as a function of the distortion u. Figure taken from [10].

as $-\frac{1}{2}Q_3 + \frac{\sqrt{3}}{2}Q_2$) and in fact, there is usually a one to one correspondence between orbitals and lattice distortions. Taking into account both distortion modes, the energy only depends on $Q_2 + Q_3$. Plotting the energy in the (Q_3, Q_2)-plane results in a rotation of the potential in Fig. 1.4 around the vertical axis, known as the "Mexican hat" potential shown in Fig. 1.5.

Here, the distortion can freely rotate in the (Q_3, Q_2)-plane, as there exists a continuum of minima, all with the same distance from the pole. However, once anharmonic corrections to the harmonic approximation are taken into account, the situation looks different. The energy now also depends on the angle $\theta = \arctan \frac{Q_2}{Q_3}$:

$$E_2 \sim \cos 3\theta. \tag{1.49}$$

For most compounds, the proportionality constant is negative, leading to minima of $\theta = 0, \pm\frac{2}{3}\pi$, which correspond to local elongations of octahedra. If the distortion modes are treated as quantum mechanical coordinates, the system can tunnel from one minimum to another, resulting in a vanishing expectation of the distortion modes. This is the case for a single JT-ion in a crystal. There are, however, still physical effects to this description, because here, in contrast to the adiabatic approximation, a particular lattice state corresponds to a particular electronic configuration, i.e. the basis states are, for example:

$$\begin{aligned} |\Psi_1\rangle &= |\psi_1\rangle\,|\phi_1\rangle\,, \\ |\Psi_2\rangle &= |\psi_2\rangle\,|\phi_2\rangle\,, \end{aligned} \tag{1.50}$$

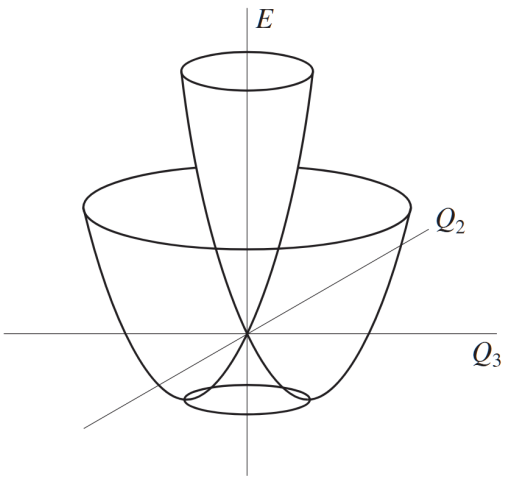

Figure 1.5: "Mexican hat" potential energy surface of the coupling between the e_g states and (Q_3, Q_2) distortion modes. Figure taken from [10].

where the $|\psi\rangle$ are the electronic and the $|\phi\rangle$ are the lattice wavefunctions. These are examples of vibronic states. Once there exists a concentration of JT-sites in a crystal, cooperative effects can occur, leading to (among other consequences) a structural phase transition. This will be described in the following subsection. The JTE is especially strong for ions with four electrons and not-too-strong crystal field splitting (leading to an occupation of orbitals according to Hund's rules and therefore one e_g electron) or nine electrons (i.e. one e_g hole) in the valence d-orbital. An example of the former case is the Mn^{3+} ion, as in $LaMnO_3$.

For now, a brief excursion to a related phenomenon, the pseudo Jahn-Teller effect shall be made. When there are orbitals that are not degenerate, but close in energy, distortions can increase the splitting of the the energy levels [18]. This effect is stronger for states that are closer in energy [18]. A schematic depiction of this mechanism for a system with two levels is shown in Fig. 1.6.

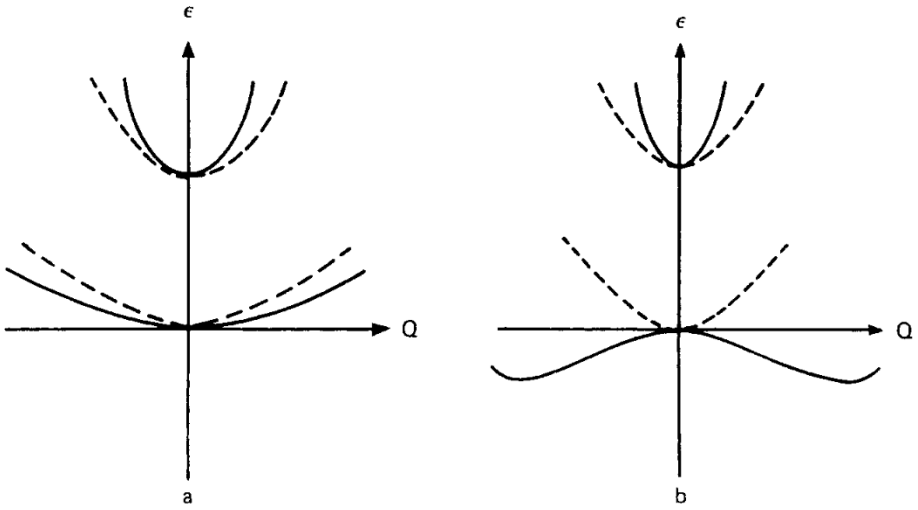

Figure 1.6: Change of energy levels due to pseudo JTE. (a) Weak PJTE - the ground state is still stable. (b) Strong PJTE - the ground state bekomes unstable. Figure taken from [14].

1.4.1 Cooperative JTE and orbital ordering

Now, the cooperative case of the Jahn-Teller effect for concentrated JT ions in crystals (CJTE) and the connected phenomenon of orbital ordering (o.o.) in the e_g case is described. This subsection takes reference from Chapter 6.1 in [10]. Orbital ordering and the CJTE always occur together. Even if the resulting phase transition is mainly driven by one of the two effects, the other one is always a consequence.

The CJTE can be described fully quantum mechanically, but here, a semiclassical explanation that yields sufficiently accurate results is given. For this it is assumed that the distortion of the JT-active site, which in many cases lowers the local symmetry, is approximated by an impurity in an elastic material. More concretely, a sphere that models the undistorted ion with high symmetry is replaced by an ellipsoid that models the local symmetry around the JT-distorted ion. In elasticity theory this leads to a strain field:

$$F(\mathbf{r}) \sim d\, Q \frac{\Gamma(\mathbf{n})}{|\mathbf{r}|^3}, \tag{1.51}$$

where d depends on the elastic moduli of the material, Q is the "strength"

of the inclusion and the angular part $\Gamma(\mathbf{n})$, with $\mathbf{n} = \mathbf{r}/|\mathbf{r}|$, leads so a field that (reduced to two dimensions) is schematically shown in Fig. 1.7.

In the case of multiple JT-sites, the distortions will form a packing that minimizes the total strain in the crystal and therefore the energy. In systems where the JT-distorted octahedra share common corners, as is the case in $LaMnO_3$, the optimal packing is that of in-phase stacked planes in which the octahedra are elongated in the x- or y-direction in a "checkerboard" pattern. Depending on the particular distortion present at one site, either the $|x^2\rangle$ or the $|y^2\rangle$ electronic state will be most favorable. The result is that the orbital occupations are ordered on correspondence with the lattice distortions - the crystal exhibits orbital ordering. Here, o.o. follows the CJTE, but the opposite can also be the case.

The e_g electrons can be described by the following Hamiltonian:

$$\mathcal{H} = \sum_{<i,j>,\alpha\beta,\sigma} -t_{ij}^{\alpha\beta} c_{i\alpha,\sigma}^{\dagger} c_{j\beta,\sigma} + \sum_{i,\alpha\sigma\neq\beta\sigma'} U_{\alpha\beta} n_{i\alpha\sigma} n_{i\beta\sigma'} - J_H \sum_i (2S_{i1}S_{i2} + \frac{1}{2}), \tag{1.52}$$

where the first sum is the tight binding approximation, the second sum is the Hubbard term that is added to tight binding and that models on-site Coulomb repulsion between electrons and the third sum is the energy gain due to Hund's rule coupling for electrons with parallel spin at the same site. i, j are site indices, $< i, j >$ indicates summation over nearest-neighbor pairs, α, β are orbital indices and σ spin indices. Assuming $U \gg t$, $U_{\alpha\beta} = U$ and that hopping is only allowed between two states with the same orbital index, the hopping term can be treated as a perturbation of the remaining Hamiltonian and the most optimal orbital occupation can be obtained by calculating the second order energy correction using perturbation theory. Looking at only one nearest-neighbor pair and one e_g electron at each site, there are four possible combinations of states. Under the supposition that the electron at site i is in state $|1\uparrow\rangle$ the electron at site j can be in these four states: $|1\uparrow\rangle, |1\downarrow\rangle, |2\uparrow\rangle, |2\downarrow\rangle$, where 1 and 2 are orbital indices. In the first case, the Pauli principle prohibits hopping and the second order energy

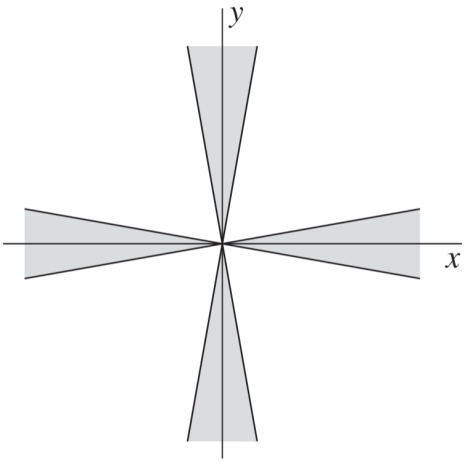

Figure 1.7: Shape of the field due to a JT-distorted ion. The light areas correspond to attraction and the dark areas to repulsion (or it is the other way round). Figure taken from [10].

correction is zero. For the second case, it is given by:

$$E_2(|1\uparrow_i,\ 1\downarrow_j\rangle) = 2t^2 \frac{|\langle 1\uparrow_i,\ 1\downarrow_j| c^\dagger_{j1\downarrow} c_{i1\downarrow} |1\uparrow_i,\ 1\downarrow_i\rangle|^2}{E_0(|1\uparrow_i,\ 1\downarrow_j\rangle) - E_0(|1\uparrow_i,\ 1\downarrow_i\rangle)}. \tag{1.53}$$

The numerator in the equation above describes hopping from state $|1\downarrow_j\rangle$ to $|1\downarrow_i\rangle$ and back. The factor 2 comes from the fact that the electron at site i can likewise hop to site j and back. For the state where the two electrons are at different sites (the first energy term in the denominator), the Hubbard and Hund's rule contributions are zero. In the case where they are at the same site (second energy term), there is the Hubbard contribution U. The energy correction therefore amounts to:

$$E_2(|1\uparrow_i,\ 1\downarrow_j\rangle) = \frac{-2t^2}{U}. \tag{1.54}$$

From an analogous calculation, one obtains the energy corrections for the third and fourth case:

$$\begin{aligned} E_2(|1\uparrow_i,\ 2\uparrow_j\rangle) &= \frac{-2t^2}{U - J_H}, \\ E_2(|1\uparrow_i,\ 2\downarrow_j\rangle) &= \frac{-2t^2}{U}. \end{aligned} \tag{1.55}$$

From this it can be seen that, in this simplified model, an antiferro-orbital and ferromagnetic ordering is lowest in energy. It is generally true that ferromagnetic ordering corresponds to antiferro-orbital ordering and vice versa. For real materials, however, the calculations are much more involved. This mechanism is called *Kugel-Khomskii superexchange*. Here, lattice distortions would follow the orbital ordering to further minimize the total energy. How CJTE and orbital ordering are realized in $LaMnO_3$ is described in chapter 3.

1.4.2 Dynamic JTE

The reference for the subsection on the dynamic JTE is taken from [8]. Recall that the e^g states are doubly degenerate for a transition metal ion with undistorted octahedral ligand configuration and that the electronic state corresponding to a particular distortion in the (Q_3, Q_2)-plane is only rotated by 90° when the distortion is rotated by 180°. For example, the electronic ground state is $|z^2\rangle$ for $(Q_3, Q_2) \sim (1, 0)$ and $|x^2 - y^2\rangle$ for $(Q_3, Q_2) \sim (-1, 0)$. This motivates the definition of so called pseudospin oparators that obey the commutation relations of real sipn operators but are invariant under time reversal. One can define these pseudospin 1/2 operators $\boldsymbol{\tau}$ such that [10]:

$$\begin{aligned} |\tau_z = 1/2\rangle &= |z^2\rangle \\ |\tau_z = -1/2\rangle &= |x^2 - y^2\rangle \end{aligned} \quad \textit{and} \quad |\tau_x = \pm 1/2\rangle = |z^2\rangle \pm |x^2 - y^2\rangle \,. \tag{1.56}$$

The JT-contribution at one site to the Hamiltonian becomes [10]:

$$V_{JT} = -g(\tau_z Q_3 + \tau_x Q_2). \tag{1.57}$$

Now, the Q_i are assumed to be quantum mechanical coordinates with conjugate momenta P_i that are affected by a harmonic potential:

$$\mathcal{H}_0 = \sum_i (P_i^2 + \omega^2 Q_i^2)/2. \tag{1.58}$$

This description now shifts to the case of a TM ion with octahedral coordination and one d-electron in a superposition of the three t_{2g} states. As mentioned in 1.1, the modes (Q_3, Q_2) split the t_{2g} energy levels. The potential energy surface of this system now depends on the strength of the spin-orbit coupling in the transition metal ion and is shown in Fig. 1.8.

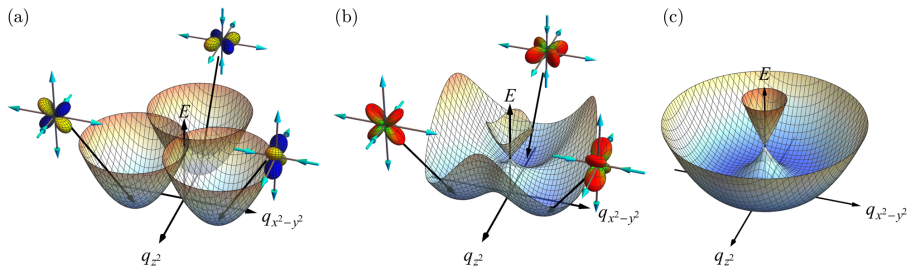

Figure 1.8: Adiabatic potential energy surface in the distortion coordinates for different strengths of spin-orbit coupling. q_{z^2} corresponds to Q_3 and $q_{x^2-y^2}$ to Q_2. The electronic ground states for the energetic minima of the distortion-modes are also indicated. (a) No spin-orbit-coupling. (b) Moderate spin-orbit coupling. (c) Strong spin-orbit coupling. The change of the adiabatic potential energy surface is due to the reduction of electron-phonon coupling by spin-orbit coupling [8]. Figure taken from [8].

There are now three approaches to describe the dynamic JTE. If the adiabatic potential energy surface (APES) takes the shape of Fig. 1.8 (b), tunneling with transfer parameter t between the three minima can occur. This leads to an overlap between the lattice states and the electronic eigenstates become:

$$\begin{aligned} |z^2\rangle &= -\frac{1}{\sqrt{6}}|xz\rangle - \frac{1}{\sqrt{6}}|yz\rangle + \frac{2}{\sqrt{6}}|xy\rangle\,, \\ |x^2-y^2\rangle &= \frac{1}{\sqrt{2}}|xz\rangle - \frac{1}{\sqrt{2}}|yz\rangle\,, \\ |A\rangle &= \frac{1}{\sqrt{3}}|xz\rangle + \frac{1}{\sqrt{3}}|yz\rangle + \frac{1}{\sqrt{3}}|xy\rangle\,. \end{aligned} \tag{1.59}$$

The states $|z^2\rangle$ and $|x^2-y^2\rangle$ form a lower lying vibronic doublet shifted by -t and should not be confused with the e_g states denoted by $|z^2\rangle$ and $|x^2-y^2\rangle$. The state $|A\rangle$ is the higher lying vibronic singlet, shifted by 2t. This effect is called *tunneling splitting*. It should, however, be noted that the total state is vibronic and each electronic state $|xy\rangle$, $|xz\rangle$ and $|yz\rangle$ corresponds to a lattice state in the respective paraboloid in Fig 1.8 (a). Since in the ground state, all three minima of the distortion have equal weight and are therefore equally likely, the expectation of the distortion vanishes and can not be detected through x-ray or neutron diffraction.

In the case of an APES like in Fig. 1.8 (c), the lattice degrees of freedom

can now rotate in the trough of the "Mexican hat" potential. The total lattice dynamics are a simultaneous rotation in the (Q_3, Q_2)-plane with "angular momentum" j and harmonic oscillations of $Q = \sqrt{Q_3^2 + Q_2^2}$. The ground state is given by:

$$|\psi(\theta)\rangle \, \chi_0(Q) e^{ij\theta}/\sqrt{2\pi}, \tag{1.60}$$

where $|\psi(\theta)\rangle$ is the adiabatic state with $\tan\theta = \frac{Q_2}{Q_3}$ and $\chi_0(Q)$ is the zero-point state of a harmonic oscillator with coordinate Q. The corresponding energy is:

$$E_j \approx -E_{JT} + \hbar\omega \left(-\frac{1}{2} + \frac{j^2}{2(g'/2)^2} \right), \tag{1.61}$$

where g' is a dimensionless quantity that measures the strength of the electron-phonon coupling. Because $|\psi(\theta)\rangle$ switches sign under $\theta \to \theta + 2\pi$, j must be half-integer, so that the total wavefunction is invariant under a rotation of 2π. In this description, the ground state is also a doublet and the first excited state is a singlet. This agrees qualitatively with the result from tunneling splitting [8].

A third approach is to numerically diagonalize the Jahn-Teller Hamiltonian, yielding the same qualitative results. The dynamic JTE can be observed in resonant inelastic x-ray scattering spectra. There, a double peak for electronic transitions that would normally indicate a broken symmetry of the ligand field can be explained by the dynamic JTE, which, at the same time, does not introduce static symmetry breaking.

The dynamic JTE has been investigated in molecular dynamics simulations before [19]. There, an analysis of the time series data of distortion modes showed a continuous dynamic alteration that was taken as proof of the dynamic nature of the JTE. Another used DFT data to construct a model Hamiltonian for the nuclei and showed the dynamic JTE via the solution of the nuclear Schrödinger equation [20].

Chapter 2

Computational methods

Density functional theory (DFT) is one of the most prominent methods in computational materials science today. The accuracy with which techniques based on DFT can predict ground state properties is unprecedented. In principle, the accuracy of forces on atoms in molecules of crystals calculated with DFT also allows to accuratly study the dynamics of such systems at different time scales using molecular dynamics. Since however, DFT calculations demand a lot of computing power, the computing times required to complete molecular dynamics simulations with a reasonable number of time steps are too large for practical purposes. One rather new method to solve this is the use of machine learning with so-called machine learned force fields (MLFF). This is the method adopted in this study. Therefore, this chapter will first provide the basics of DFT. Then, some information on the molecular dynamics algorithm will be given. Last, the machine learned force field method will be explained. All the calculations in this study have been conducted using the Vienna Ab Initio Simulation Package (VASP) [21, 22, 23] with the projector-augmented wave (PAW) method [24].

2.1 Density functional theory

In this section, the basic theory of density functional theory shall be described. At its core lies the approach that quantities, such as for example the energy, can be expressed as functionals of the electronic density in a material. Finding the ground state electronic density would then yield the ground state energy of a system. In most cases, this is significantly less complex than finding the many-body wavefunction [25]. The latter part of this section (subsections 2.1.2 and 2.1.3) shall be devoted to the description of specific machine lerning techniques used in the present study.

2.1.1 From the Thomas-Fermi model to the Kohn-Sham equations

The first example of a model that makes use of the idea of calculating the electron density is the Thomas-Fermi model for the electronic distribution in a heavy atom, developed in two papers from 1926 by L. Thomas [26] and 1928 by E. Fermi [27]. Thomas starts with the assumptions that [26]:

- Relativistic effects are negligible.
- Inside the atom, there is a field with potential V, such that
  - $V \to 0$ as $r \to \infty$ and
  - $rV \to const$ as $r \to 0$.
- Electrons are distributed uniformly in the six-dimensional phase space, with two electrons occupying a phase space volume of h^3.
- V is determined by the charge of the nucleus and the electronic distribution itself.

He sets up the (single-electron) Hamiltonian:

$$\mathcal{H} = \frac{p^2}{2m} - eV, \tag{2.1}$$

where e is the elementary charge. Reference for the following quantitative derivation is taken from [25]. Dividing the space into small cubes with volume $\Delta V = l^3$ that each contain a specific individual number of non-interacting electrons and assuming that these cubes do not interact with each other, the cubes can be described as infinite three dimensional potential wells of width l with energies ($\hbar = 1$, $m = 1$):

$$\epsilon(n_x, n_y, n_z) = \frac{\pi^2}{2l^2}(n_x^2 + n_y^2 + n_z^2) = \frac{\pi^2}{2l^2}R^2, \tag{2.2}$$

with n_x, n_y andn_z positive integers. For large R, the number of states with energy less than or equal to $\epsilon(R)$ is the volume of one eigth of a sphere with radius R:

$$\Phi(\epsilon) = \frac{\pi R^3}{6} = \frac{\Delta V}{6\pi^2}(2\epsilon)^{3/2}. \tag{2.3}$$

This gives the density of states:

$$g(\epsilon)\delta\epsilon = \Phi(\epsilon + \delta\epsilon) - \Phi(\epsilon) = \frac{\Delta V}{\pi^2}\sqrt{\frac{\epsilon}{2}}\delta\epsilon. \tag{2.4}$$

To compute the total energy, the probability distribution of a state being occupied by an electron, depending on ϵ, is needed. For fermions, this is the Fermi-Dirac distribution, which, for zero Kelvin is:

$$f(\epsilon) = \begin{cases} 1 & \epsilon < \epsilon_F, \\ 0 & \epsilon > \epsilon_F. \end{cases} \tag{2.5}$$

The total energy and number of electrons in a given cube with volume ΔV are given by:

$$\Delta E = 2\int_0^\infty g(\epsilon)f(\epsilon)\epsilon d\epsilon = \frac{\Delta V}{10\pi^2}(2\epsilon_F)^{5/2}, \tag{2.6}$$

$$\Delta N = 2\int_0^\infty g(\epsilon)f(\epsilon)d\epsilon = \frac{\Delta V}{3\pi^2}(2\epsilon_F)^{3/2}. \tag{2.7}$$

The factor of two in both equations comes from the fact that two electrons can occupy any given state. The energy can be written in terms of ΔN and then in terms of the electron density $\rho = \frac{\Delta N}{\Delta V}$ as:

$$\begin{aligned} \Delta E &= \frac{\Delta V}{10\pi^2}\left(\frac{3\pi^2\Delta N}{\Delta V}\right)^{5/3} \\ &= \frac{3^{5/3}\pi^{4/3}\Delta V}{10}\rho^{5/3}. \end{aligned} \tag{2.8}$$

Calculation the total kinetic energy across the whole atom now amounts to summing up all the ΔE. For $\Delta V \to 0$, $\rho \to \rho(\mathbf{r})$ and the summation becomes an integration over the three spatial dimensions:

$$T_{TF}[\rho] = C_{TF} \int d^3 r \rho^{5/3} \quad \text{with} \quad C_{TF} = \frac{3^{5/3}\pi^{4/3}}{10}. \tag{2.9}$$

With 2.1, the total energy as a functional of the electron density becomes:

$$E_{TF}[\rho] = T_{TF}[\rho] - Z \int d^3 r \frac{\rho(\mathbf{r})}{r} + \frac{1}{2} \int d^3 r_1 d^3 r_2 \frac{\rho(\mathbf{r}_1)\rho(\mathbf{r}_2)}{|\mathbf{r}_1 - \mathbf{r}_2|}, \tag{2.10}$$

where Z is the atomic number of the nucleus and the factor of one half in front of the last term takes into account double counting. Under the assumption that the ground state distribution minimizes the energy, this equation can be solved by using the variational principle and requiring that the integral of the electronic density over the whole space is the total number of electrons in the atom. The Thomas-Fermi model does not predict molecular binding and is otherwise inaccurate. This is because the assumption of a non-interacting electron gas is a very crude approximation.

The foundation for proper DFT was laid by P. Hohenberg and W. Kohn in 1964 when they proved two theorems that allow to express the energy as an exact functional of the electron density[28]. The starting point is the Hamiltonian for a number of electrons indexed with i:

$$\mathcal{H} = \sum_i \frac{-\nabla_i^2}{2} + \frac{1}{2} \sum_{i \neq j} \frac{1}{r_{ij}} + \sum_i V(\mathbf{r}_i), \tag{2.11}$$

where $V(\mathbf{r})$ is an external potential and for which the following variational principle holds for the ground state energy E_0 and any trial wavefunction Ψ:

$$E_0 \leq \langle \Psi | \mathcal{H} | \Psi \rangle . \tag{2.12}$$

The explanation again follows [25]. The first Hohenberg-Kohn theorem shows that the external potential $V(\mathbf{r})$ is uniquely determined by the electron density, with the exception of an additive constant. This can be seen through the following consideration: For a non-degenerate ground state with density $\rho(\mathbf{r})$, assume that there are two distinct potentials $V(\mathbf{r})$ and $V'(\mathbf{r})$ that differ

by more than a constant and that are associated with different Hamiltonians $\mathcal{H}$ and $\mathcal{H}'$ as well as different ground state wavefunctions Ψ and Ψ'. Then, by the variational principle, one can set up two inequalities:

$$\begin{aligned} E_0 < \langle \Psi' | \mathcal{H} | \Psi' \rangle &= \langle \Psi' | \mathcal{H}' | \Psi' \rangle + \langle \Psi' | \mathcal{H} - \mathcal{H}' | \Psi' \rangle \\ &= E_0' + \int d^3 r \rho(\mathbf{r})(V(\mathbf{r}) - V'(\mathbf{r})) \end{aligned} \tag{2.13}$$

and

$$\begin{aligned} E_0' < \langle \Psi | \mathcal{H}' | \Psi \rangle &= \langle \Psi | \mathcal{H} | \Psi \rangle + \langle \Psi | \mathcal{H}' - \mathcal{H} | \Psi \rangle \\ &= E_0 + \int d^3 r \rho(\mathbf{r})(V'(\mathbf{r}) - V(\mathbf{r})). \end{aligned} \tag{2.14}$$

Adding the two inequalities yields $E_0 + E_0' < E_0' + E_0$, which is a contradiction. If the two potentials only differ by a constant, then they are not associated to different wavefunctions and one can not set up the two inequalities.

The second theorem by Hohenberg and Kohn establishes that the ground state density does in fact minimize the energy. Due to the first theorem, any distribution $\tilde{\rho}$ is uniquely associated with its potenial , Hamiltonian and wavefunction $\tilde{V}$, $\tilde{\mathcal{H}}$ and $\tilde{\Psi}$, which we can take as a trial wave function. ρ shall be the ground state density. Then:

$$\begin{aligned} E_V[\rho] = E_0 \leq \langle \tilde{\Psi} | \mathcal{H} | \tilde{\Psi} \rangle \\ = F_{HK}[\tilde{\rho}] + \int d^3 r \tilde{\rho}(\mathbf{r}) V(\mathbf{r}) = E_V[\tilde{\rho}]. \end{aligned} \tag{2.15}$$

Here, $F_{HK}[\tilde{\rho}]$ denotes the part of the energy that does not depend on the external potential but only the density, namely the kinetic energy and electron-electron interaction. Since it does not depend on $V(\mathbf{r})$, it is called a *universal functional*. These theorems justifiy the use of the variational principle for the Thomas-Fermi model and show that it is an approximation of DFT. The densities used in the proofs need to be *V-representable*, which means that they are a density associated with an antisymmetric ground state wave function of the Hamiltonian in 2.11. They can, however, be generalized for *N-representable* densities (densities that are associated to possible antisymmetric N-particle

wavefunctions) with the following requirements:

$$\begin{aligned} \rho(\mathbf{r}) &\geq 0, \\ \int d^3r \rho(\mathbf{r}) &= N, \\ \int d^3r |\nabla \rho^{1/2}(\mathbf{r})|^2 &< \infty. \end{aligned} \tag{2.16}$$

Further, it is possible to weaken the requirement of a non-degenerate ground state.

The following description of the Kohn-Sham equations again takes reference from [25]. The main idea that was introduced by W. Kohn and L. J. Sham in 1965 is that one can map the exact problem of multiple interacting electrons in an external potential to the problem of non-interacting electrons in a different *effective potential* [29]. One can seperate the universal functional F:

$$F[\rho] = T_s[\rho] + J[\rho] + E_{xc}[\rho], \tag{2.17}$$

where T_s is the kinetic energy of a non-interacting electron gas:

$$T_s[\rho] = \left\langle \Psi_s \left| \sum_{i=1}^{N} \frac{-\nabla^2}{2} \right| \Psi_s \right\rangle = \sum_{i=1}^{N} \left\langle \Psi_i \left| \frac{-\nabla^2}{2} \right| \Psi_i \right\rangle. \tag{2.18}$$

Here, Ψ_s is the antisymmetric ground state of a *non-interacting* electron system with some external potential and the Ψ_i are the single-electron wavefunctions. J is the Coulomb electron-electron repulsion that is also included in the Thomas-Fermi model:

$$J[\rho] = \frac{1}{2} \int d^3r_1 d^3r_2 \frac{\rho(\mathbf{r}_1)\rho(\mathbf{r}_2)}{|\mathbf{r}_1 - \mathbf{r}_2|}. \tag{2.19}$$

E_{xc} includes exchange and correlation effects. Expressing ρ as a sum of single-particle densities:

$$\rho(\mathbf{r}) = \sum_{i=1}^{N} |\psi_i(\mathbf{r})|^2, \tag{2.20}$$

one can write down an effective potential as:

$$V_{eff}(\mathbf{r}) = V(\mathbf{r}) + \frac{\delta J[\rho]}{\delta \rho} + \frac{\delta E_{xc}[\rho]}{\delta \rho} = V(\mathbf{r}) + \int d^3r_1 \frac{\rho(\mathbf{r}_1)}{|\mathbf{r} - \mathbf{r}_1|} + V_{xc}(\mathbf{r}). \tag{2.21}$$

From this, one obtains the Kohn-Sham equations, which can be solved self-consistently:

$$\left[\frac{-\nabla_i^2}{2} + V_{eff}\right]\psi_i = \epsilon_i^{KS}\psi_i, \tag{2.22}$$

where the Kohn-Sham orbitals ψ_i have no pyhsical meaning and the total energy is not the sum of the Kohn-sham eigenenergies:

$$E_0 = \sum_{i=1}^{N} \epsilon_i^{KS} - J[\rho] + E_{xc}[\rho] - \int d^3r \rho(\mathbf{r}) V_{xc}(\mathbf{r}). \tag{2.23}$$

The ϵ_i^{KS} are in fact the energies needed to insert an extra electron into the system [30]:

$$\frac{\partial E}{\partial n_i} = \epsilon_i^{KS}. \tag{2.24}$$

n_i is the occupation number of the i-th Kohn-Sham orbital.

So far, everything has been dealt with exactly. However, the explicit form of the exchange-correlation functional is unknown. Several different methods to approximate it have been proposed and the quality of a DFT-calculation depends on how well the approximation of the exchange-correlation functional works for the system in question. The *local density approximation* (LDA) is the simplest method and was introduced by Kohn and Sham themselves [25]:

$$E_{xc}^{LDA}[\rho] = \int d^3r \rho(\mathbf{r}) \epsilon_{xc}[\rho(\mathbf{r})]. \tag{2.25}$$

Here, $\epsilon_{xc}[\rho]$ is the exchange-correlation energy of a uniform electron gas with density ρ. The so called *generalized gradient approximation* (GGA) is an improvement upon the LDA. In this approximation, the gradient of the density is taken into account as well [25]:

$$E_{xc}^{GGA}[\rho] = \int d^3r \rho(\mathbf{r}) \epsilon_{xc}[\rho(\mathbf{r}), \nabla\rho(\mathbf{r})]. \tag{2.26}$$

The specific exchange-correlation functionals used in the calculations for this study are a flavor of GGA and were introduced by Perdew, Burke and Ernzerhof (hence these functionals are called PBE functionals) [31].

2.1.2 Spin polarization and constrained noncollinear magnetic moments

To predict magnetic ordering phenomena with DFT, it is necessary to take into account electron spins. This is done in spin-DFT by replacing the Kohn-Sham orbitals with 2-spinors as suggested by the Dirac equation [32]. The following description takes reference from [32]. From the 2-spinors $\mathbf{\Psi}_i(\mathbf{r})$ one constructs a charge density $\rho(\mathbf{r})$ and a spin density $\mathbf{s}(\mathbf{r})$:

$$\begin{aligned} \rho(\mathbf{r}) &= \sum_i \mathbf{\Psi}_i^\dagger(\mathbf{r})\mathbf{\Psi}_i(\mathbf{r}), \\ \mathbf{s}(\mathbf{r}) &= \sum_i \mathbf{\Psi}_i^\dagger(\mathbf{r})\mathbf{S}(\mathbf{r})\mathbf{\Psi}_i(\mathbf{r}). \end{aligned} \tag{2.27}$$

Here, $\mathbf{S}$ is the spin operator. The universal functional $F[\rho]$ is then replaced by a functional $G[\rho, \mathbf{s}]$ that takes into account the spin density. Writing:

$$\mathbf{\Psi}_i(\mathbf{r}) = \phi_i(\mathbf{r}, 1)\chi_\uparrow + \phi_i(\mathbf{r}, 2)\chi_\downarrow, \tag{2.28}$$

one obtains for charge and spin density (with $\hbar = 1$):

$$\begin{aligned} \rho(\mathbf{r}) &= \sum_i |\phi_i(\mathbf{r}, 1)|^2 + |\phi_i(\mathbf{r}, 2)|^2, \\ s_x(\mathbf{r}) &= \mathrm{Re} \sum_i \phi_i^*(\mathbf{r}, 1)\phi_i(\mathbf{r}, 2), \\ s_y(\mathbf{r}) &= \mathrm{Im} \sum_i \phi_i^*(\mathbf{r}, 1)\phi_i(\mathbf{r}, 2), \\ s_z(\mathbf{r}) &= \sum_i |\phi_i(\mathbf{r}, 1)|^2 - |\phi_i(\mathbf{r}, 2)|^2. \end{aligned} \tag{2.29}$$

Introducing the density matrix:

$$n_{\alpha\beta}(\mathbf{r}) = \sum_i \sum_i \phi_i^*(\mathbf{r}, \alpha)\phi_i(\mathbf{r}, \beta), \tag{2.30}$$

one obtains for the charge and spin density:

$$\begin{aligned} \rho(\mathbf{r}) &= \mathrm{Tr}[n], \\ \mathbf{s}(\mathbf{r}) &= \frac{1}{2} \sum_{\alpha\beta} n_{\alpha\beta}(\mathbf{r})\boldsymbol{\sigma}_{\alpha\beta}. \end{aligned} \tag{2.31}$$

$\boldsymbol{\sigma}$ are the Pauli matrices. Using the variational principle and the exchange correlation potentials $V^{xc}_{\alpha\beta}$, one obtains an equivalent to the Kohn-Sham equations:

$$\left[\frac{-\nabla^2}{2} + V(\mathbf{r}) + \frac{\delta J[\rho]}{\delta \rho}\right]\phi_i(\mathbf{r},\alpha) + \sum_\beta V^{xc}_{\alpha\beta}(\mathbf{r})\phi_i(\mathbf{r},\beta) = \epsilon_{i,\alpha}\phi_i(\mathbf{r},\alpha). \quad (2.32)$$

Defining an *effective magnetic field* $\mathbf{B}_{xc}$ by:

$$V_{xc} := \frac{V^{xc}_{11} + V^{xc}_{22}}{2}, \quad B^{xc}_x := \frac{V^{xc}_{12} + V^{xc}_{21}}{2\mu_B}, \quad B^{xc}_y := i\frac{V^{xc}_{12} - V^{xc}_{21}}{2\mu_B}, \quad B^{xc}_z := \frac{V^{xc}_{11} - V^{xc}_{22}}{2\mu_B}, \quad (2.33)$$

leads to the compact equation:

$$\left[\frac{-\nabla^2}{2} + V(\mathbf{r}) + \frac{\delta J[\rho]}{\delta \rho} + V_{xc}(\mathbf{r}) + \mu_B \boldsymbol{\sigma}\mathbf{B}_{xc}(\mathbf{r})\right]\boldsymbol{\Psi}_i(\mathbf{r}) = \epsilon_i \boldsymbol{\Psi}_i(\mathbf{r}). \quad (2.34)$$

Often, it is enough to approximate the spins as collinear. To include spin-orbit coupling in a DFT-calculation or to predict exotic magnetic ordering like in BNOO, this does not suffice. For the calculations with BNOO that were conducted for this study, the directions of the magnetic moments were constrained to previous results from DFT that are reported in chapter 4. To do this in VASP, a penalty energy is included [33]:

$$E_M = \sum_I \lambda \left[\mathbf{M}_I - \mathbf{M}^0_I(\mathbf{M}^0_I\mathbf{M}_I)\right]^2. \quad (2.35)$$

Here, λ, which sets the strength of the constraint and the $\mathbf{M}^0_I$, which are the desired magnetic moments, are set as tags in the INCAR file of the VASP input. One can also constrain the direction and size of the magnetic moments, which is done with the penalty energy [33]:

$$E_M = \sum_I \lambda \left[\mathbf{M}_I - \mathbf{M}^0_I\right]^2, \quad (2.36)$$

or the direction and sign.

2.1.3 Dudarev's +U correction

Dudarev's +U correction is a way to include an effective on-site Coulomb interaction like in the Hubbard model [34]. It was introduced as an extension of LSDA, but is applied to PBE functionals in this study. With this

correction, the correct order of magnitude of the band gap of for example NiO can be predicted, something that is impossible for LSDA alone [34]. The present explanation follows the original work by Dudarev et al. [34].

The Hamiltonian:

$$\mathcal{H}^U = \frac{U}{2} \sum_{m,m',\sigma} \hat{n}_{m,\sigma} \hat{n}_{m',-\sigma} + \frac{U-J}{2} \sum_{m \neq m',\sigma} \hat{n}_{m,\sigma} \hat{n}_{m',\sigma}, \tag{2.37}$$

is considered to approximate the effective on-site interaction of d-electrons. The total energy functional then becomes:

$$E^{LSDA+U}[\rho] = E^{LSDA}[\rho] + E^U[\rho] + E^{dc}[\rho], \tag{2.38}$$

where E^{dc} is the double counting functional to account for the part of the energy correction that is already included in standard LSDA [35]. With the assumption that $E^{dc} = E^U$ in the atomic limit (which means integer occupations of the d-orbitals, since there is no exchange of electrons with a surrounding system) one obtains:

$$E^{dc} = \frac{U}{2} \sum_{\sigma} N_\sigma N_{-\sigma} + \frac{U-J}{2} \sum_{\sigma} N_\sigma (N_\sigma - 1), \tag{2.39}$$

where N_σ is the total number of d-electrons with spin projection σ. For the more general case of non-integer N_σ, one obtains from the unrestricted Hartree-Fock approximation:

$$E^U = \frac{U}{2} \sum_{m,m',\sigma} n_{m,\sigma} n_{m',-\sigma} + \frac{U-J}{2} \sum_{m \neq m',\sigma} n_{m,\sigma} n_{m',\sigma}. \tag{2.40}$$

Subtracting the above equations, one obtains the energy correction:

$$E^{LSDA+U} = E^{LSDA} + \frac{U-J}{2} \sum_{m,\sigma} n_{m,\sigma} - n_{m,\sigma}^2. \tag{2.41}$$

Here, U and J only enter as a difference and can be denoted by a single parameter U_{eff}. This parameter can be set in VASP.

2.2 Molecular Dynamics

In this section, the integrator for the equations of motion, namely the *velocity Verlet algorithm*, and the form of the *Langevin thermostat* that is used to sample the NpT ensemble are described. With these ingredients, the forces in a system that are caluclated with DFT are used to simulate the time evolution of the system in molecular dynamics (MD) runs.

2.2.1 Velocity-Verlet algorithm

First, the implementation of the velocity Verlet algorithm shall be described. Then, it shall be shown that this integrator can be derived from a certain partition of the Liouville operator as a time reversible integrator. The reference for the description of the velocity Verlet integrator is taken from [36] and this scheme is equivalent to the one described on the VASP wiki [33]. For a system with an arbitrary number of degrees of freedom, Newton's equation of motion is:

$$\ddot{\mathbf{r}} = \mathbf{f}(\mathbf{r}), \tag{2.42}$$

where $\mathbf{f}(\mathbf{r})$ is the vector that one obtains by element-wise division of the force components by the masses of the corresponding degrees of freedom. For a discrete integration with time step Δt the following notation is used:

$$\begin{aligned} t_n &= n\Delta t, \\ \mathbf{r}_n &= \mathbf{r}(t_n), \\ \dot{\mathbf{r}}_n &= \dot{\mathbf{r}}(t_n). \end{aligned} \tag{2.43}$$

Using the approximations:

$$\begin{aligned} \dot{\mathbf{r}}_n &\approx (\mathbf{r}_{n+1} - \mathbf{r}_{n-1})/(2\Delta t), \\ \ddot{\mathbf{r}}_n &\approx (\mathbf{r}_{n+1} - 2\mathbf{r}_n + \mathbf{r}_{n-1})/\Delta t^2, \end{aligned} \tag{2.44}$$

the standard Verlet algorithm can be written down as:

$$\mathbf{r}_{n+1} = 2\mathbf{r}_n - \mathbf{r}_{n-1} + \Delta t^2 \mathbf{f}(\mathbf{r}_n). \tag{2.45}$$

The velocity is then defined by:

$$\mathbf{v}_n := (\mathbf{r}_{n+1} - \mathbf{r}_{n-1})/(2\Delta t). \tag{2.46}$$

A better way to implement this for calculations with finite precision is to let the velocity enter the equations explicitly with the scheme:

$$\begin{aligned} \mathbf{r}_{n+1} &= \mathbf{r}_n + \mathbf{v}_n \Delta t + \mathbf{f}(\mathbf{r}_n)\Delta t/2, \\ \mathbf{v}_{n+1} &= \mathbf{v}_n + (\mathbf{f}(\mathbf{r}_{n+1}) + \mathbf{f}(\mathbf{r}_n))\Delta t/2. \end{aligned} \tag{2.47}$$

This is equivalent to the implementation described on the VASP wiki [33]:

$$\begin{aligned} \mathbf{v}_{n+1/2} &= \mathbf{v}_n + \mathbf{f}(\mathbf{r}_n)\Delta t/2, \\ \mathbf{r}_{n+1} &= \mathbf{r}_n + \mathbf{v}_{n+1/2}\Delta t, \\ \mathbf{v}_{n+1} &= \mathbf{v}_{n+1/2} + \mathbf{f}(\mathbf{r}_{n+1})\Delta t/2. \end{aligned} \tag{2.48}$$

The derivation of the velocity Verlet algorithm follows [37]. For a system with with N degrees of freedom and Hamiltonian $\mathcal{H}$, the Liouville operator is:

$$i\mathcal{L} = \{\cdots, \mathcal{H}\} = \sum_{i=1}^{N} \left[\dot{r}_i \frac{\partial}{\partial r_i} + F_i \frac{\partial}{\partial p_i} \right]. \tag{2.49}$$

Here, $\{\cdots, \cdots\}$ denotes the Poisson bracket and $\Gamma(t) = \{r_i(t), p_i(t)\}$ is the state of the system in phase space at a time t. The propagator of the system is then:

$$U(t) = e^{i\mathcal{L}t}, \tag{2.50}$$

which means that:

$$\Gamma(t) = U(t)\Gamma(0). \tag{2.51}$$

Splitting the Liouville operator into two parts:

$$i\mathcal{L} = i\mathcal{L}_1 + i\mathcal{L}_2 \tag{2.52}$$

and writing $t = P\Delta t$, the following identity holds due to the Trotter theorem [38]:

$$e^{i\mathcal{L}t} = \left(e^{i\mathcal{L}_1 \Delta t/2} e^{i\mathcal{L}_2 \Delta t} e^{i\mathcal{L}_1 \Delta t/2}\right)^P + \mathcal{O}(\Delta t^2 t). \tag{2.53}$$

Therefore, the propagation for a small time step ΔT can be approximated by:

$$G(\Delta t) = e^{i\mathcal{L}_1 \Delta t/2} e^{i\mathcal{L}_2 \Delta t} e^{i\mathcal{L}_1 \Delta t/2}, \tag{2.54}$$

and G is unitary and consequently the propagation is time reversible:

$$G^{-1}(t) = G(-t). \tag{2.55}$$

Using the explicit splitting:

$$\begin{aligned} i\mathcal{L}_2 &= \dot{\mathbf{r}}\nabla_{\mathbf{r}}, \\ i\mathcal{L}_1 &= \mathbf{F}(\mathbf{r})\nabla_{\mathbf{p}}, \end{aligned} \tag{2.56}$$

one obtains:

$$e^{i\mathcal{L}_2\Delta t}\{\mathbf{r},\mathbf{p}\} = \{\mathbf{r}+\dot{\mathbf{r}}\Delta t,\mathbf{p}\}, \tag{2.57}$$

because $\mathcal{L}_2$ is just the Liouville operator of free propagation. Similarly, one obtains:

$$e^{i\mathcal{L}_1\Delta t}\{\mathbf{r},\mathbf{p}\} = \{\mathbf{r},\mathbf{p}+\mathbf{F}(\mathbf{r})\Delta t\}. \tag{2.58}$$

Putting everything together, and using $v_i = \dot{r}_i = p_i/m_i$ as well as $f_i = F_i/m_i$ the propagation can be approximated by:

$$\begin{aligned} &e^{i\mathcal{L}\Delta t}\{\mathbf{r},\mathbf{p}\} \approx \\ &\approx \{[\mathbf{r}+\mathbf{v}\Delta t+\mathbf{f}\Delta t^2/2],[\mathbf{p}+(\mathbf{F}(\mathbf{r})+\mathbf{F}(\mathbf{r}+\mathbf{v}\Delta t+\mathbf{f}\Delta t^2/2))\Delta t/2]\}, \end{aligned} \tag{2.59}$$

which is precisely the velocity Verlet algorithm. The velocity Verlet algorithm is also symplectic and therefore preserves phase space volume [39]. It shall be noted that a Hamiltonian system was implicitly assumed for this derivation. The equations of motion of the Langevin thermostat described below do not correspond to a Hamiltonian and the integration becomes time irreversible and non-symplectic.

2.2.2 Langevin thermostat and the NpT ensemble

To maintain constant temperature, the MD runs are carried out using a *Langevin thermostat* as described on the VASP wiki [33]. The equations of motion are adapted to include a friction term and a statistical force term like the Langevin equation:

$$\begin{aligned} \dot{r}_i &= p_i/m_i, \\ \dot{p}_i &= f_i - \gamma_i p_i + \phi_i. \end{aligned} \tag{2.60}$$

ϕ_i is a random force chosen from a normal distribution with variance:

$$\sigma_i^2 = 2m_i\gamma_i k_B T/\Delta t. \tag{2.61}$$

The NpT ensemble is sampled by considering the lattice vectors as additional degrees of freedom with a fictitious mass that obey the equations of motion

and are under an external stress that corresponds to some pressure [33]. This is called the *Parinello-Rahman algorithm* [40]. For the present study, hydrostatic stress was used.

2.3 Machine learned force fields

DFT calculations are computationally demanding. The sizes for supercells, i.e. the number of atoms in a simulation, and the time scales that are needed to investigate certain phenomena lead to unreasonable computation times for MD simulations where the forces are calculated with DFT at every time step [1]. A way to solve this problem is to use *machine learned force fields* (MLFF) that are trained on DFT data and can then predict energy, forces and stress tensor (EFS) for longer MD runs with larger supercells [1]. This machine learning approach is a built in feature of VASP and how it is realized is described in this section.

2.3.1 On-the-fly training

Here, the general approach of on-the-fly training is explained. A difficulty that arises when training a force field is the selection of the set of configurations for which to conduct DFT computation. Optimally, this set should contain information of the whole phase space of the system. To choose configurations that fulfill this requirement is complex and one often has to resort to trial and error [1]. With on-the-fly training, up tp 99% of DFT calculations can be skipped already during training [1] This allows for a quicker exploration of the phase space. The reference for the following description is taken from [2].

On-the-fly training loops through a series of steps to conduct a MD simulation and simultaneously train a force field. If an existing force field is supplied as input, it is used from the start of the simulation. Otherwise a new force field is created. The mentioned steps are:

1. If there is already an existing force field (either supplied as an input of created during previous MD steps of the same simulation), the energy,

forces and stress tensor are calculated from the force field for the present structure.

2. VASP decides whether a DFT calculation is executed. How this decision is made is described in subsection 2.3.3. If this decision is positive, the computer continues with step 3, otherwise it skips to step 5.

3. The DFT calculation for the present structure is carried out. The resulting data is stored as potential new training data.

4. If the set of potential new training data reaches a certain size or the estimated uncertainty of the prediction is too high, a new force field is generated including the newly copllected data.

5. MD step is carried out according to the algorithms described in section 2.2. If the force field has been judged reliable, its predictions are used. Else, the results from the DFT calculation are used. Then, VASP jumps to step 1 and continues this cycle until the specified number of MD steps has been reached.

2.3.2 Machine learning approach and descriptors

Again following [2], the approach of force field training implementedin VASP shall now be described. For each atom in a structure dataset with EFS from DFT (such a structure dataset is called a *reference structure dataset*), one can extract a local configuration around the atom. These local configurations are called *local reference configurations*. The potential energy of a structure can then be approximated as a sum of local energies around each atom:

$$U = \sum_{i}^{N_a} U_i. \tag{2.62}$$

The local energies:

$$U_i = F[\rho_i(\mathbf{r})], \tag{2.63}$$

are functionals of the local distribution of atoms around the atom in question:

$$\rho_i(\mathbf{r}) = \sum_{i}^{N_a} f(|\mathbf{r}_i - \mathbf{r}_j|)\delta(\mathbf{r} - (\mathbf{r}_i - \mathbf{r}_j)), \tag{2.64}$$

where f is a smooth function that removes information outside a cutoff radius R_{cut}. This introduces an approximation, since the potential energy of the central atom generally also depends on the configuration of atoms outside of R_{cut}. VASP utilizes the *smooth overlap of atomic positions* (SOAP), for which the delta function is replaced by a gaussian function:

$$g(\mathbf{r}) = \frac{1}{\sqrt{2\sigma_{atom}\pi}} \exp\left(\frac{-|\mathbf{r}|^2}{2\sigma_{atom}^2}\right). \tag{2.65}$$

Since expanding the local distribution function in a finite basis and rewriting the functional $F[\rho_i]$ as a function of the coefficient would yield a function that is not rotationally invariant, one defines two rotationally invariant functions called *descriptors*:

$$\begin{aligned} \rho_i^{(2)}(r) &:= \frac{1}{4\pi} \int \rho_i(r\hat{\mathbf{r}}) d\hat{\mathbf{r}}, \\ \rho_i^{(3)}(r,s,\theta) &:= \int\int \delta(\hat{\mathbf{r}}\hat{\mathbf{s}} - \cos\theta) \rho_i(r\hat{\mathbf{r}}) \rho_i^*(s\hat{\mathbf{s}}) d\hat{\mathbf{r}} d\hat{\mathbf{s}}. \end{aligned} \tag{2.66}$$

Here, a hat denotes a unit vector. $\rho_i^{(2)}$ contains only radial information and is called radial distribution function, while $\rho_i^{(3)}$ contains also angular information and is called angular distribution function. Expanding $\rho_i(\mathbf{r})$ in terms of radial basis functions $\chi_{nl}(r)$ and spherical harmonics $Y_{lm}(\hat{\mathbf{r}})$:

$$\rho_i(\mathbf{r}) = \sum_{l=1}^{L_{max}} \sum_{m=-l}^{l} \sum_{n=1}^{N_R^l} c_{nlm}^i \chi_{nl}(r) Y_{lm}(\hat{\mathbf{r}}), \tag{2.67}$$

one can write down the descriptors in this way:

$$\begin{aligned} \rho_i^{(2)}(r) &= \frac{1}{\sqrt{4\pi}} \sum_{n=1}^{N_R^0} c_n^i \chi_{nl}(r), \\ c_n^i &= c_{n00}^i, \\ \rho_i^{(3)}(r,s,\theta) &= \sum_{l=1}^{L_{max}} \sum_{n=1}^{N_R^l} \sum_{\nu=1}^{N_R^l} \sqrt{\frac{2l+1}{2}} p_{n\nu l}^i \chi_{nl}(r) \chi_{\nu l}(s) P_l(\cos\theta), \\ p_{n\nu l}^i &= \sqrt{\frac{8\pi^2}{2l+1}} \sum_{m=-l}^{l} c_{nlm}^i c_{\nu lm}^{i*}. \end{aligned} \tag{2.68}$$

Here, P_l are Legendre polinomials of degree l. For N_B local reference configurations and having the vectors $\mathbf{X}_i$ contain all the coefficients c^i_{nlm} and $p^i_{n\nu l}$, the functional for the local potential energy is approximated by:

$$U_i = F[\rho_i^{(2)}, \rho_i^{(3)}] = \sum_{i_B=1}^{N_B} w_{i_B} K(\mathbf{X}_i, \mathbf{X}_{i_B}), \tag{2.69}$$

where K measures the similarity between a local configuration for which the local potential energy shall be calculated and a local reference configuration. The w_{i_B} are a set of weights. The explicit form of K can be found in [2], but it does not influence the following explanations and is therefore omitted here. The optimal values for the weights are now to be found by fitting the EFS of a set of reference structure datasets, each with its own number of local reference configuration. The specific method for this is described in the following section 2.3.3.

2.3.3 Error estimation with Bayesian linear regression

Again taking reference from [2], the fitting of the weights wi_B and the estimation of the uncertainties of the precdictions, both done by Bayesian linear regression, shall be described. Finally, an additional quantity the *spilling factor* is described and it is briefly explained how the decision whether to perform a DFT calculation is made.

Starting from the assumption that there is a set of weights that predicts the EFS exactly. Then, for a finite number of reference structure datasets that contain numerical noise, the probability that a given set of weights is the optimal one is calculated. The following notation is adopted:

$\mathbf{y}^\alpha$ is a vector containing the EFS for one reference structure dataset with index α. $\mathbf{Y}$ is a vector containing all EFS for all reference structure datasets in the training set. $\mathbf{w}$ is a vector containing the weights w_{i_B} and $\boldsymbol{\phi}^\alpha$ is a vector that contains $\sum_i K(\mathbf{X}_i, \mathbf{X}_{i_B})$ in the first row and partial derivatives with respect to structure coordinates in the others. $\boldsymbol{\Phi}$ is the vector that contains all $\boldsymbol{\phi}^\alpha$.

The posterior probability $p(\mathbf{w}|\mathbf{Y})$ to find the optimal weights at $\mathbf{w}$ under

the condition of the labels $\mathbf{Y}$ is written as a Gaussian distribution:

$$\begin{aligned} p(\mathbf{w}|\mathbf{Y}) &= \mathcal{N}(\bar{\mathbf{w}}, \mathbf{\Sigma}), \\ \bar{\mathbf{w}} &= \frac{1}{\sigma_v^2}\mathbf{\Sigma}\mathbf{\Phi}^T\mathbf{Y}, \\ \mathbf{\Sigma}^{-1} &= \frac{1}{\sigma_w^2}\mathbf{I} + \frac{1}{\sigma_v^2}\mathbf{\Phi}^T\mathbf{\Phi}. \end{aligned} \tag{2.70}$$

Here, $\mathbf{I}$ is the identity and σ_v^2 and σ_w^2 are hyperparameters. $\mathcal{N}$ denotes a multivariate Gaussian. From this it can be seen that the optimal set of weights coincides with $\bar{\mathbf{w}}$. Since for a new structure, the EFS are obtained by:

$$\mathbf{y} = \boldsymbol{\phi}\mathbf{w}, \tag{2.71}$$

the posterior distribution of this becomes:

$$\begin{aligned} p(\mathbf{y}|\mathbf{Y}) &= \mathcal{N}(\boldsymbol{\phi}\mathbf{w}, \boldsymbol{\sigma}), \\ \boldsymbol{\sigma} &= \sigma_v^2\mathbf{I} + \mathbf{\Phi}^T\mathbf{\Sigma}\mathbf{\Phi}. \end{aligned} \tag{2.72}$$

Since here, the second summand in the second equation corresponds to the uncertainty of $\mathbf{w}$, this can be used to decide whether a new DFT calculation should be carried out. In practice, the Bayesian error of the force-components in the EFS-vector $\mathbf{y}$ is used. The above mentioned spilling factor is defined as:

$$s = 1 - \frac{\sum_{i_B=1}^{N_B}\sum_{i'_B=1}^{N_B} K(\mathbf{X}, \mathbf{X}_{i_B})K^{-1}(\mathbf{X}_{i_B}, \mathbf{X}_{i'_B})K(\mathbf{X}_{i'_B}, \mathbf{X})}{K(\mathbf{X}, \mathbf{X})}, \tag{2.73}$$

and serves as a measure of the density of local reference configurations around a new local configuration. If the overlap is large, the fraction becomes close to 1 and the spilling factor close to zero. as the density of local reference configurations decreases, the spilling factor grows to 1. For a new structural dataset, the spilling factors are written as a vector $\mathbf{s}$. To decide whether a DFT-calculation shall be carried out, two thresholds, one for the Bayesian error of the forces and one for $\mathbf{s}$, are used. The threshold for the Bayesian errors of the forces is updated on-the fly, while the threshold for the spilling factor is set to 0.02. If the maximum of the force uncertainties or the maximum spilling factor exceed double their respective thresholds, a DFT calculation is

performed always. Otherwise, if ten MD steps have passed since the last DFT loop, a new calculation is performed if the maxima exceed their respective thresholds. Else, the DFT calculation is skipped.

Chapter 3

The perovskite $LaMnO_3$

$LaMnO_3$ (LMO) is a perovskite containing Mn^{3+} ions at the centers of the oxygen octahedra. It has an orthorhombic structure with Pbnm space group and lattice parameters $a = 5.5367(1)$ Å, $b = 5.7473(1)$ Å, $c = 7.6929(2)$ Å at room temperature [5]. In this setting, the unit cell contains four formula units [41]. In its low-T phase it exhibits a cooperative JTE with associated orbital ordering [5]. At $T_1 = 750$ K it undergoes a phase transition and the domains of cooperative structural distortions shrink, while orbital ordering disappears [5, 4]. Due to steric $GdFeO_3$-type octahedral tilts, the orthorhombic Pbnm symmetry persits, but the lattice becomes metrically cubic with $a \approx 5.58$ Å, as reported in a high resolution newtron-powder diffraction study [5]. Only the Q_2 and Q_3 distortions described above have been reported to be active. The octahedra exhibit long, medium and short bond lengths with values $l = 2.178(1)$ Å, $m = 1.9680(3)$ Å and $s = 1.907(1)$ Å at room temperature [5]. The O-Mn-O bond angles are $2 \times 90.4(8)°$, $2 \times 89.6(8)°$, $2 \times 90.5(8)°$, $2 \times 89.5(8)°$, $2 \times 90.6(2)°$, $2 \times 89.4(2)°$ and $3 \times 180°$ at room temperature and $6 \times 91.0(1)°$, $6 \times 89.0(1)°$ and $3 \times 180°$ at T = 1273 K [41].

Fig. 3.1 shows a $\sqrt{2}a \times \sqrt{2}b \times c$ supercell rotated by 45° around the c-axis, which consists of eight formula units.

LMO is one of the typical examples with a CJTE and orbital ordering

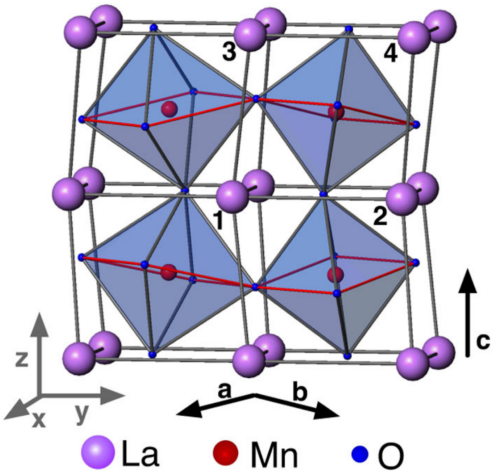

Figure 3.1: Structure of LMO in the orthorhombic Pbnm setting. Figure taken from [42].

[10]. As its Mn^{3+} ions have $3d^4$ configuration, there is strong interaction between the doubly degenerate Q_2 and Q_3 modes and the doubly degenerate e_g orbitals. The Jahn-Teller Problem in LMO is the one described in 1.4. A fully quantum mechanical theory of the CJTE in LMO based on electron-phonon coupling would yield $\tan\theta = \frac{Q_2}{Q_3} = \pm 60°$, where the orbital state is given by $|\theta\rangle = \cos\theta/2\,|z^2\rangle + \sin\theta/2\,|x^2 - y^2\rangle$ [10]. The superexchange mechanism described in section1.4.1 that gives rise to orbital ordering leads to a theoretical prediction of $\theta = \pm 90°$ [10]. However, anharmonic effects change the situation and lead to a mixing angle that is closer to $\pm 120°$, which is local elongation of the octahedra in the x- and y- directions [10]. Experimentally, LMO exhibits $\theta \approx 108°$ at room temperature [5]. A consequence of this is that the Mn-O bond lengths separate into long, medium and short, as mentioned above. Further, the e_g orbitals are not rotationally symmetric around the longest axis, but their lobes in the other two directions are different in size (see Fig. 3.2) [10]. This stabilizes ferromagnetic ordering in the x-y plane and antiferromagnetic ordering in the z (or c) direction, since superexchange between different z planes is only allowed for different spins, as this direction has ferro-orbital ordering. In total, this is A-type antiferromagnetic ordering which is experimentally observed below $T_N = 140$ K [43].

Above $T_1 = 750$ K, the situation is more complicated. Experimen-

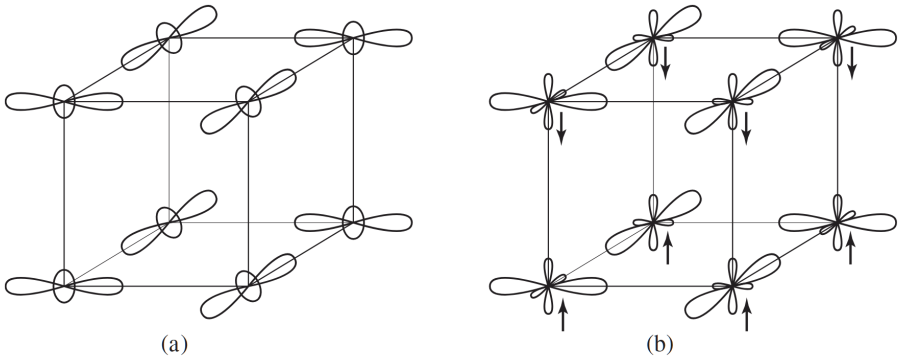

Figure 3.2: Orbital ordering in LMO. (a) Schematic representation with rotationally symmetric orbitals. (b) Closer to the real shape of the orbitals. The arrows indicate the direction of the Mn magnetic moments. Figure taken from [10].

tal data suggests that the JT distortions are significantly weakened in this phase, with $\frac{2(l-s)}{l+s}$ dropping from 11 % to 2.4 % [42]. θ becomes ≈ 90 °, as indicated by Mn-O bond lengths and orbital mixing parameters [5]. It has, however, been confirmed that the transition is order-to-disorder and that the distortions remain fully active locally up to at least $T \approx 1150$ K [42, 4]. Even the ordering persists locally, as the orbital correlation length is roughly 16 Å or 4 MnO_6 octahedra [4]. A calculation of the Kugel-Khomskii transition temperature in LMO yields $T_{KK} \approx 550$ K, so the explanation of this phenomenon must take into account electron-phonon coupling, which is not included in the simulation methods described in Chapter 2 [42]. The fact that the lattice becomes pseudocubic above T_1 has been attributed to dynamic effects [5].

A good choice for the Hubbard U correction has been shown to be $U = 3.5$ eV [44]. In line with this, $U_{eff} = 3.5$ eV was chosen for most calculations with LMO in this study. There have been studies with different choices [45, 46, 47], but this value has been used to reproduce the low-T phase of LMO in machine learned molecular dynamics simulations [3]. Calculations of the magnetic moments of the manganese ions have yielded values between 3 and 4 μ_B [48]. Therefore, and again following a previous study [3], the Mn magnetic moments were initialized as 4 μ_B in an A-type antiferromagnetic ordering.

Some have claimed that LMO is not JT-active at all [49]. The authors of this study argue that the strong hybridization between the manganese 3d and oxygen 2p orbitals leads to significant delocalization of the e_g electrons. This prevents a JT instability and orbital ordering. According to them, orbital ordering is established in systems with what they call a Q_2^- distortion where the z planes are stacked out of phase but not in systems with a Q_2+ mode (z planes stacked in phase) like in LMO. The octahedral distortions would then be explained by purely classical steric considerations due to the octahedral tilts.

Chapter 4

The double perovskite Ba_2NaOsO_6

Ba_2NaOsO_6 (BNOO) is a double perovskite with a rock-salt ordering of the Na^+ and Os^{7+} cations at the centers of oxygen octahedra [50]. Powder X-ray diffraction experiments show, that it has an fcc structure with $Fm\bar{3}m$ space group and a lattice parameter of $a = 8.28566(5)$ Å at room temperature [50]. This unit cell is shown in Fig. 4.1.

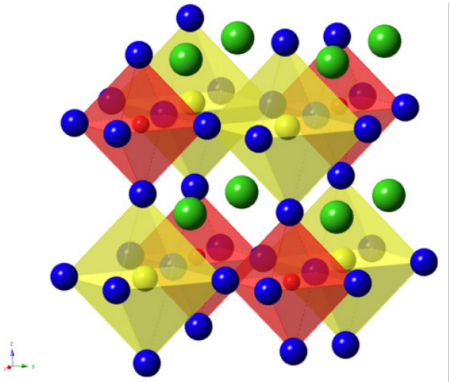

	x	y	z
Ba	0.25	0.25	0.25
Na	0	0	0
Os	0.5	0.5	0.5
O	0.2256	0	0

Figure 4.1: Unit cell of BNOO with 40 atoms. Figure taken from [**Cong**].

4.1 Physical properties of Ba_2NaOsO_6

The Os^{7+} ions have $5d^1$ electronic configuration and exhibit strong spin-orbit coupling [7]. The electronic correlation (Hubbard U) makes BNOO an insulator rather than a metal [12]. Such insulators in which the band gap arises from electronic correlation are called *Mott insulators*. In line with a previous study on the lattice, orbital and magnetic ground state of BNOO [7], an effective Coulomb interaction of $U_{eff} = 3.4$ eV was used in the present study, while a tight-binding analysis yielded $U \approx 3.3$ eV [12].

Below $T_c \approx 6.3$ K, BNOO is reported to exhibit local magnetic moments of around $0.2\mu_B$. DFT + U + SOC calculations[7] utilizing constrained magnetic moments have shown that this is in fact a canted antiferromagnetic (cAFM) ordering with local magnetic moments form an angle of $\phi \approx \pm 67°$ with the common "ferromagnetic" direction. This ordering is realized by ferromagnetic planes stacked antiferromagnetically. Since the canting angle is $> 45°$, the magnetic ground state is closer to AFM ordering than FM ordering - hence the nomenclature of cAFM. This ground state is stabilized by Jahn-Teller distortions that also alternate antiferro-like, corresponding

to the directions of the local magnetic moments. Omitting JT distortions, a canted ferromagnetic phase cFM is stabilized [7]. The described ground state is shown in Fig. 4.2.

It has been found with the help of nuclear magnetic resonance that BNOO undergoes a phase of so called *broken local point symmetry* (BLPS) upon cooling that preceeds magnetic ordering [11, 6, 51]. The corresponding phase transition is of thermodynamic nature [6]. Calculations of electric field gradient tensors and connected quadrupolar moments explain these results with the emergence of local Q_2 distortions in the BLPS phase, but additional octahedral rotations have not been ruled out [52, 53]. Since BNOO remains cubic at low T, as found by X-ray diffraction [12], a dynamic JTE has been proposed [13]. However, the two-sublattice cAFM magnetic ground state corresponds to a two-sublattice orbital ordering in the low temperature phase [54].

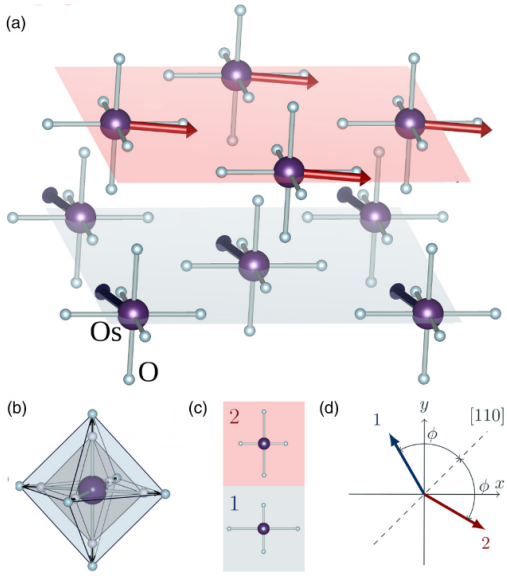

Figure 4.2: Ground state magnetic ordering with connected JT-distortions in BNOO. Figure taken from [7].

4.2 The Jahn-Teller problem in Ba_2NaOsO_6

Since the osmium ions in BNOO have $5d^1$ electronic configuration, the 5d electron will occupy one of the t_{2g} orbitals or a linear combination of them. As mentioned in section 1.1, the t_{2g} states are not only split by the orthorhombic and tetragonal distortions that have been labeled Q_2 and Q_3 above, but also by trigonal distortions. Following the paper by Van Vleck that introduces these normal coordinates Q_i [55], the first six are defined in the following way, with the numbering convention of the ligand atoms shown in Fig. 4.3:

$$\begin{aligned}
Q_1 &= (X_2 - X_5 + Y_3 - Y_6 + Z_1 - Z_4)/\sqrt{6}, \\
Q_2 &= (X_2 - X_5 - Y_3 + Y_6)/2, \\
Q_3 &= (2Z_1 - 2Z_4 - X_2 + X_5 - Y_3 + Y_6)/(2\sqrt{3}), \\
Q_4 &= (Y_2 - Y_5 + X_3 - X_6)/2, \\
Q_5 &= (X_1 - X_4 + Z_2 - Z_5)/2, \\
Q_6 &= (Z_3 - Z_6 + Y_1 - Y_4)/2.
\end{aligned} \tag{4.1}$$

Here, the X_i, Y_i and Z_i denote displacements of atom i from its high symmetry position in the x- y- or z-direction. Q_1 does not lower the local symmetry

around the transition metal ion, but denotes an expansion or contraction of the whole octahedron. It is active in BNOO, as can be seen from Fig. 4.2 (b).

Now, due to strong spin-orbit coupling, the 5d t_{2g} states in BNOO split into a spin doublet denoted by Γ_6 and a spin quadruplet denoted by Γ_8, as described in chapter 3.3 of [14]. In BNOO, the effective J for spin-orbit coupling at the osmium sites is 3/2 and the ground state is the Γ_8 quadruplet [7, 13]. It couples due to the Jahn-Teller theorem to both the doubly degenerate modes (Q_2, Q_3) and the triply degenerate modes (Q_4, Q_5, Q_6) [14]. Such a Jahn-Teller problem is denoted by $\Gamma_8 \otimes (e + t_2)$, where, following the notation in chapter 3 of [14], the lower case letters denote the symmetry representations of nuclear displacements. The energy in the five-dimensional space of the ionic distortion modes is then [14]:

$$\epsilon_{\pm}(\rho, Q) = \frac{1}{2}(K_E\rho^2 + K_T Q^2) \pm (F_E^2\rho^2 + F_T^2 Q^2)^{\frac{1}{2}}, \tag{4.2}$$

where $\rho^2 = Q_2^2 + Q_3^2$ and $Q^2 = Q_4^2 + Q_5^2 + Q_6^2$. The K_E and K_T are the forces of the harmonic approximation for the doubly and triply degenerate distortion modes respectively. The F_E and F_T are the linear electron-phonon coupling coefficients. Now, the two couplings $\Gamma_8 \otimes e$ and $\Gamma_8 \otimes t_2$ have different JT energies [14]:

$$\begin{aligned} E_{JT}^E &= \frac{F_E^2}{2K_E}, \\ E_{JT}^T &= \frac{F_T^2}{2K_T}, \end{aligned} \tag{4.3}$$

and the resulting minima will depend on which JT energy is larger. If $E_{JT}^E > E_{JT}^T$, then [14]:

$$\rho^0 = \frac{F_E}{K_E}, \quad Q^0 = 0, \tag{4.4}$$

while if $E_{JT}^E < E_{JT}^T$, then [14]:

$$\rho^0 = 0, \quad Q^0 = \frac{F_T}{K_T}. \tag{4.5}$$

The other three coordinates, which can in this case be understood as angles, become a three-dimensional trough where free rotation is possible [14]. In the

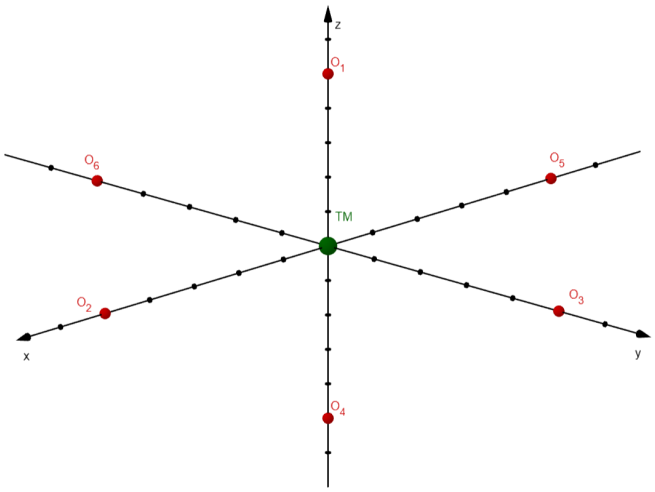

Figure 4.3: Numbering of the ligand oxygen ions for the definition of the Van Vleck normal coordinates.

case of (4.4), the adiabatic potential energy surface reduced to the (Q_3, Q_2) space is a mexican hat (compare Fig. 1.8 (c)). If $E^E_{JT} = E^T_{JT}$, there is an additional trough in the (ρ, Q) space [14].

Chapter 5

Results

The orbital ordering phase transition in LMO has been observed in MD simulations utilizing MLFF before [3]. The principal results of this study were reproduced and constant temperature production runs were conducted to deepen the understanding of the simulated phase transition. To this end, analyses on the level of individual MnO_6 octahedra and correlations across the supercell were carried out. Furthermore, the Van Vleck modes Q_4, Q_5 and Q_6 as well as octahedral rotations were investigated. Additionally some findings on the dynamics of various degrees of freedom are reported below. As a next step, the methodology was applied to BNOO. For the training of the MLFF, some DFT-parameters were amended to account for non-collinear ordering of magnetic moments, spin-orbit coupling and different electronic correlation characterized by U_{eff}. The analyses of the molecular dynamics production runs with different constant temperatures focused on the same quantities as for LMO, namely individual site and supercell characterisics of Q_2 to Q_6 and octahedral rotations, as well as some dynamical quantities.

The formulae used for all calculations in this chapter are found in appendix A. Octahedral rotations are characterized by a three-component "rotation vector". For the definition of this vector, refer to appendix B. For the calculation of the Van Vleck distortion modes and the octahedral rotations, the python package VanVleckCalculator [56, 57] was used.

5.1 LMO

The first step for this study was to reproduce the results on LMO from [3], using the supplemental material of this study as reference. Following [3], a $\sqrt{2}a \times \sqrt{2}b \times c$ supercell rotated by 45° around the c-axis was used for the training of the machine learned force field. Half of this supercell is displayed in Fig. 3.1 and it consists of eight formula units. For the production runs, this supercell was repeated three times in each direction, leading to a supercell with 216 formula units, or 1080 atoms. Force fields were trained for $U_{eff} = 0, 2, 3.5$ eV. Common to all training runs is a $4 \times 4 \times 4$ k-point grid and an energy cutoff (ENCUT) $E_{cut} = 500$ eV. The magnetic moments were initialized in A-type antiferromagnetic order with magnetic moments of 4 μ_B at the Mn sites. For the molecular dynamics simulations, time steps of 0.5 fs and 2 fs were chosen for the training and the production runs, respectively. The training run was conducted as a linear temperature ramp between 600 K and 1100 K, which, for a total simulation length of 125000 steps, is equivalent to a heating rate of 8 K/ps. The cutoff radius for the radial descriptor was chosen to be 6 Å and the cutoff radius for the angular descriptor was 5 Å. Production runs were carried out for a linear temperature ramp between 100 K and 1100 K with a heating rate of 2 K/ps and for constant temperatures of 100 K, 400 K, 600 K, 700 K, 800 K and 900 K. As mentioned above, the Perdew-Burke-Ernzerhof scheme [31] was used for the approximation of the exchange-correlation potential and the Langevin thermostat and the Parinello-Rahman algorithm were used during MD simulations.

First, the effect of different U_{eff} was analyzed. Fig. 5.1 shows the time series of the supercell averages of the Q_2- and Q_3-modes as well as the magnitude of the octahedral rotations during the temperature ramp. For all further analyses, a value of $U_{eff} = 3.5$ eV was used. Further, the 216 Mn-ions in the supercell were each assigned an index from 0 to 215 to enable an accurate specification of quantities calculated below. Fig. 5.2 to 5.4 show a) the distribution of Q_2 and Q_3 across the supercell, b) their site-site corraletions and c) the frequencies of specific values on heat maps for different temperatures T = 100 K, 600 K and 900 K. At T = 600 K,

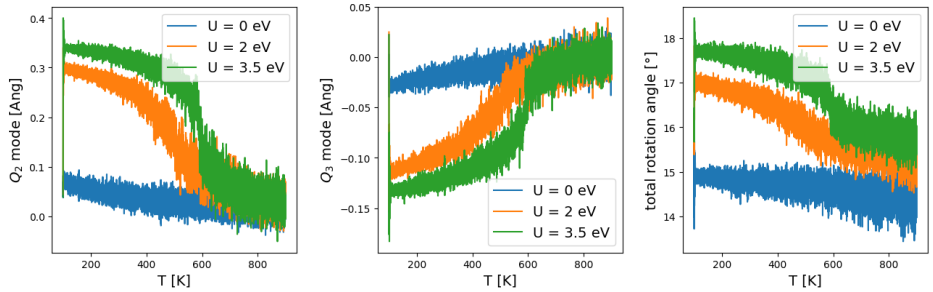

Figure 5.1: LMO during T-ramp: averages of distortions of all octahedra in the supercell. Left: absolute value of Q_2-mode. Middle: Q_3-mode. Right: Magnitude of octahedral rotation.

the correlation length of Q_2 grows to at least the diameter of the supercell (with a Pearson correlation coefficient [62] of $r \approx 0.18 - 0.2$ across the entire supercell, visualized in Fig. 5.3 b)), which implies a situation at or close to a critical temperature of a phase transition. The magnitude of Q_2 (0.34 Å at T = 100 K) and Q_3 (-0.12 Å at T = 100 K) decreases with temperature and is not significantly different from zero at T = 900 K, in accordance with Fig. 5.1. The type of ordering agrees with experimental results [41, 5], the reference study [3] and is what has been called Q_2^+ in section 3. Q_2 does not decrease to zero upon heating, but remains weakly active at high temperatures.

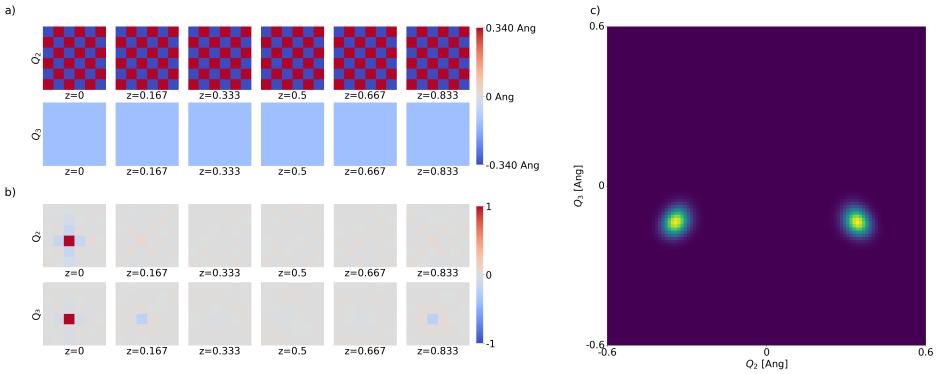

Figure 5.2: LMO at $T = 100K$: a) averages of JT-modes Q_2 and Q_3 for each octahedron around an Mn-site. b) Pearson correlation coefficients of JT-modes for each site wrt. site with index 12. c) Heat map of occurrences of JT distortion values across time and entire supercell. Brighter colors indicate a higher probability of an octahedron having a given distortion.

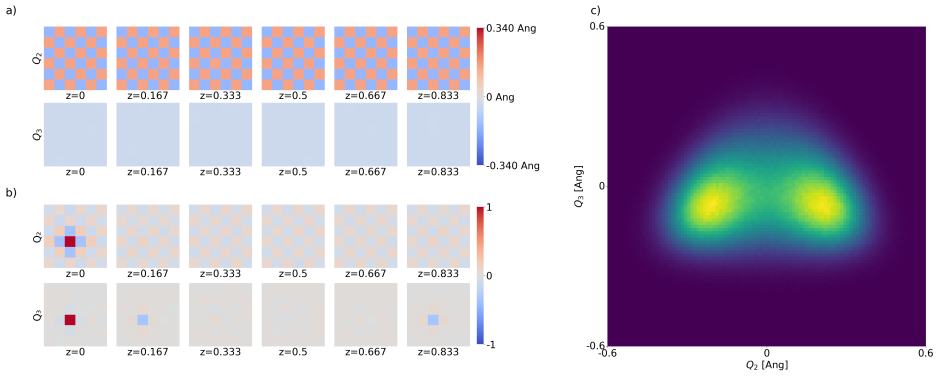

Figure 5.3: LMO at $T = 600K$: a) averages of JT-modes Q_2 and Q_3 for each octahedron around an Mn-site. b) Pearson correlation coefficients of JT-modes for each site wrt. site with index 12. c) Heat map of occurrences of JT distortion values across time and entire supercell. Brighter colors indicate a higher probability of an octahedron having a given distortion.

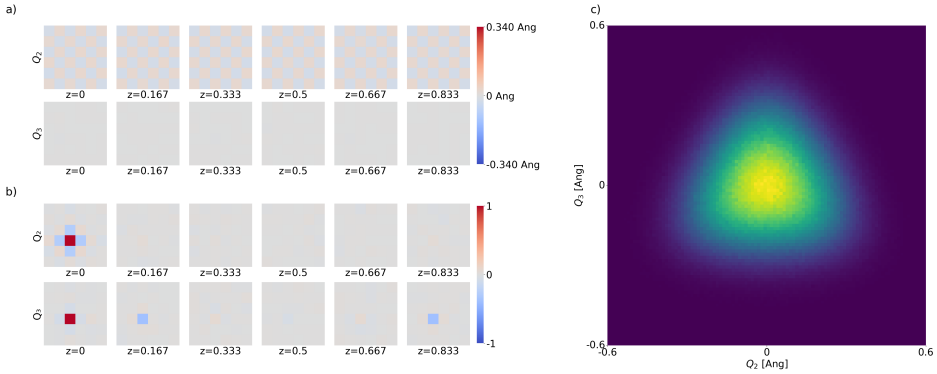

Figure 5.4: LMO at $T = 900K$: a) averages of JT-modes Q_2 and Q_3 for each octahedron around an Mn-site. b) Pearson correlation coefficients of JT-modes for each site wrt. site with index 12. c) Heat map of occurrences of JT distortion values across time and entire supercell. Brighter colors indicate a higher probability of an octahedron having a given distortion.

Fig. 5.5 shows the probability densities for the instantaneous value of Q_2 across the supercell and the entire time series for different temperatures. For low T, positive and negative values of $\pm$ 0.3 Å to 0.4 Å are most common, while above T = 600 K, Q_2 is mostly around 0 Å.

Q_4, Q_5 and Q_6 are also active, as can be seen from Fig. 5.6 to 5.8. Like above, these figures show a) the distribution of modes across the supercell,

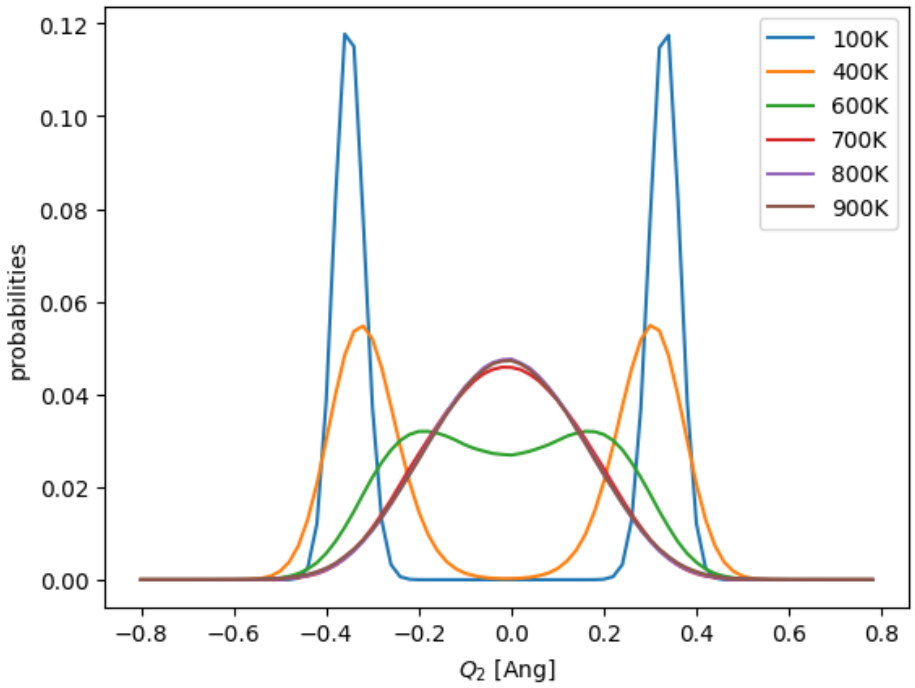

Figure 5.5: Distribution of Q2 mode in LMO for different temperatures.

b) their site-site corraletions and c) the frequencies of specific values on heat maps for different temperatures T = 100 K, 600 K and 900 K, but now for Q_4, Q_5 and Q_6. From the definition of the modes in chapter 4 it can be seen that this implies O-Mn-O bond angles that differ from 90° or 180°, which seems to contradict the experiment [41], because bond angles have been reported to be exactly 90° or 180°. The computational reference study [3] does not report data for these modes. At low T, the particular values of the modes at a given site are connected to the direction of the rotational axis of the octahedron. As shown in experiments [41, 5], there are four different directions that the average rotational axis of an octahedron can have in LMO, and these are ordered in a particular way. This has been reproduced in the present study but is not shown. The point is that each of the four rotational directions correspond to one of the four possible configurations that Q_4, Q_5 and Q_6 take at low T, which could imply that this is an artefact from octahedral rotations but at least suggests a connection to the directions of the octahedral rotation axes. The magnitudes of these modes decreases

with temperature, but a significant increase of correlation length was not found at any of the investigated temperatures, which implies that this is not a real phase transition.

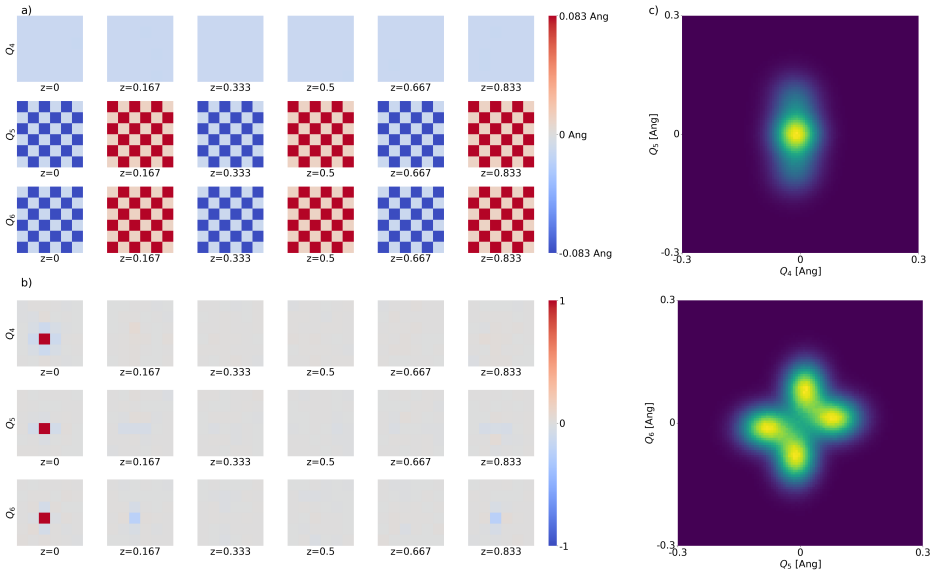

Figure 5.6: LMO at $T = 100K$: a) averages of JT-modes Q_4, Q_5 and Q_6 for each octahedron around an Mn-site. b) Pearson correlation coefficients of JT-modes for each site wrt. site with index 12. c) Heat map of occurrences of JT distortion values across time and entire supercell. Brighter colors indicate a higher probability of an octahedron having a given distortion.

To analyze the dynamics of the distortions compared to single atoms, velocity-autocorrelation functions and integrated velocity-autocorrelation times have been calculated for Q_2 to Q_5, octahedral rotations and cartesian coordinates of single La-atoms. The results of this analysis are shown in Fig. 5.9 to 5.12. The velocity-autocorrelation function of Q_2 and Q_3 exhibits significant fluctuations at T = 100 K. These fluctuations are not present at or above T = 600 K. Furthermore, the integrated velocity-autocorrelation time decreases significantly with temperature for all analyzed distortions. For the La-atoms, the fluctuations of the velocity-autocorrelation function are at a significantly larger time scale than for the distortion modes. Furthermore, these fluctuations are weakened but persist above T= 600 K. The integrated velocity-autocorrelation time of the lanthanum degrees of free-

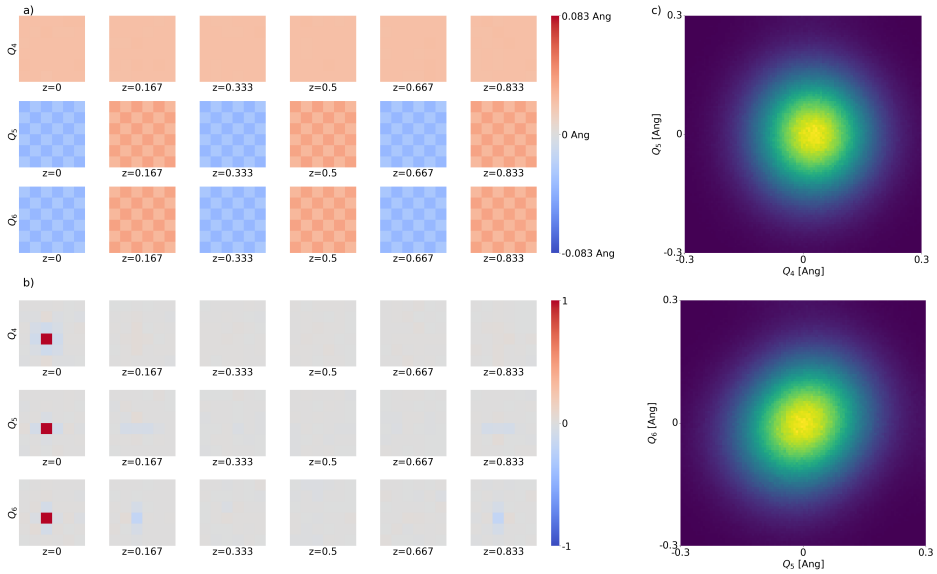

Figure 5.7: LMO at $T = 600K$: a) averages of JT-modes Q_4, Q_5 and Q_6 for each octahedron around an Mn-site. b) Pearson correlation coefficients of JT-modes for each site wrt. site with index 12. c) Heat map of occurrences of JT distortion values across time and entire supercell. Brighter colors indicate a higher probability of an octahedron having a given distortion.

dom decreases with temperature, but this decrease (relative to the integrated velocity-autocorrelation time at T = 100K) is much less than for the distortion modes. The fact that the integrated velocity-autocorrelation times of the La-ions and the distortion modes are of similar magnitude at low temperature implies that it takes these quantities a similar amount of time to lose information about their previous velocities. The lower frequency oscillations of the La-ions can be explained by the larger mass of Lanthanum compared to oxygen. Upon heating, the distortion modes transition to a thermal regime (in which all information about previous velocities is lost nearly instantly) much quicker than the La-ions. This is signified by the fact that the integrated velocity-autocorrelation time of the La-ions remains more than twice as large than that of the distortion modes at high temperatures.

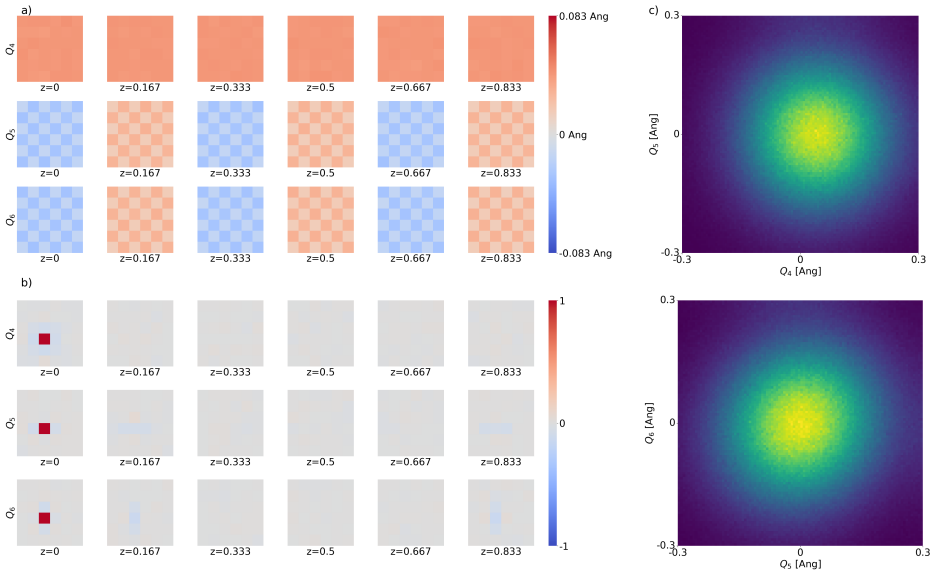

Figure 5.8: LMO at $T = 900K$: a) averages of JT-modes Q_4, Q_5 and Q_6 for each octahedron around an Mn-site. b) Pearson correlation coefficients of JT-modes for each site wrt. site with index 12. c) Heat map of occurrences of JT distortion values across time and entire supercell. Brighter colors indicate a higher probability of an octahedron having a given distortion.

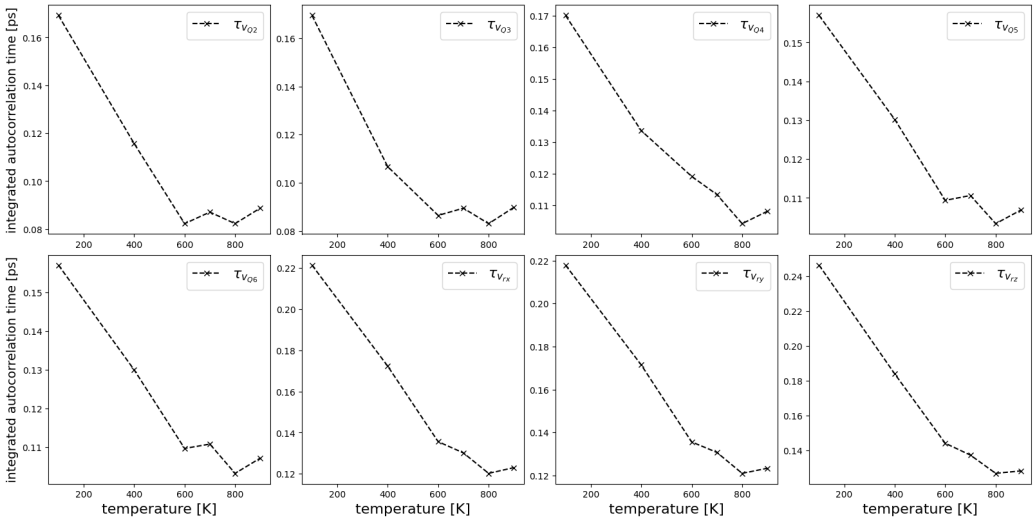

Figure 5.9: LMO: Velocity-autocorrelation times of all Van Vleck modes and octahedral rotations as functions of temperature. The dashed lines are only guides for the eyes.

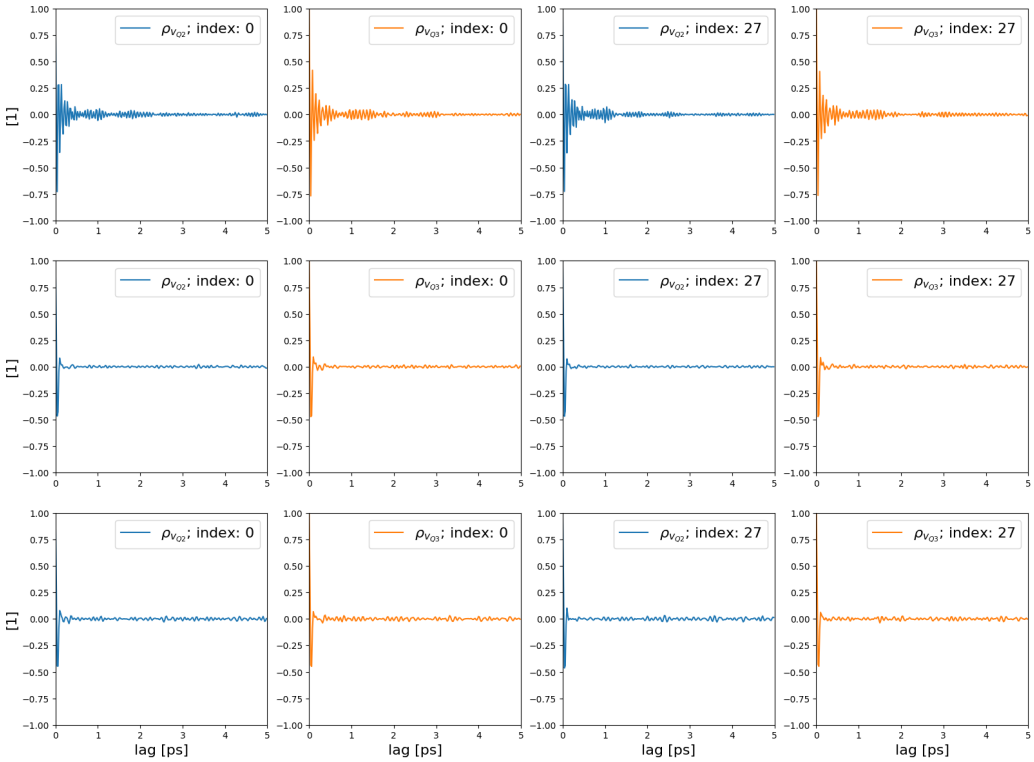

Figure 5.10: LMO: Velocity-autocorrelation functions of Q2 and Q3 for indices 0 and 27 for: top row: T = 100K; middle row: T= 600K; bottom row: T = 900K. x-axis: t [ps]

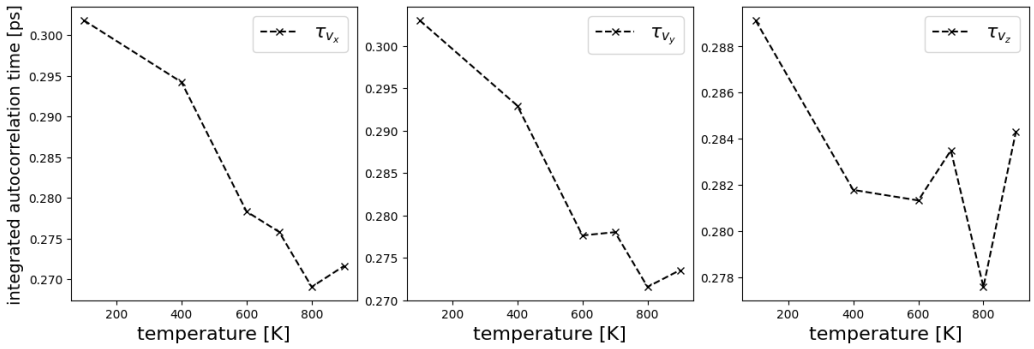

Figure 5.11: LMO: Velocity-autocorrelation times of La DOF as functions of temperature. The dashed lines are only guides for the eyes.

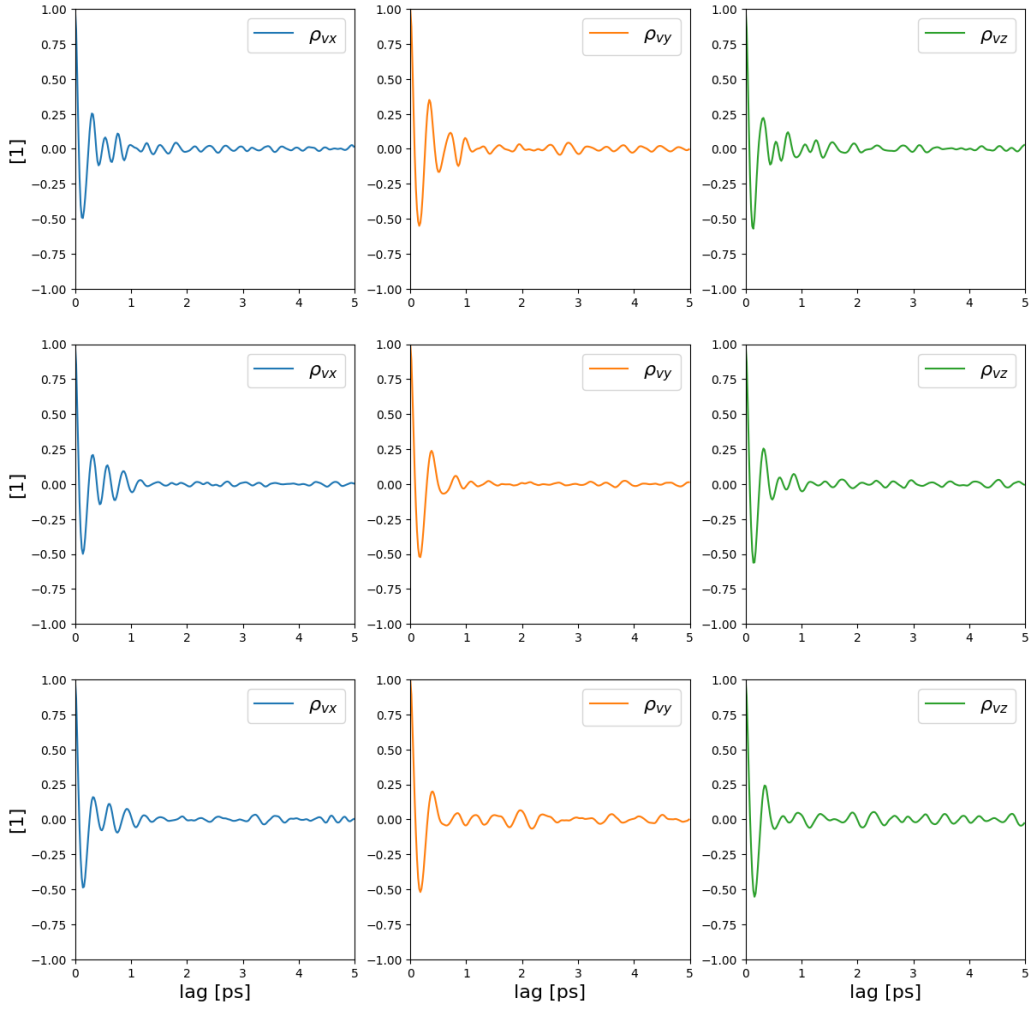

Figure 5.12: LMO: Velocity-autocorrelation functions of DOF of one La-ion for: top row: T = 100K; middle row: T= 600K; bottom row: T = 900K. x-axis: t [ps]

5.2 BNOO

For the training of the force field for BNOO, the smaller supercell described in section 4 was used. For the production runs, this unit cell was extended twice in each direction, leading to a $3\times3\times3$ supercell containing 108 formula units, or 1080 atoms. Convergence tests led to the choice of a $5\times5\times5$ k-point grid and an energy cutoff E_{cut} = 600 eV. In line with a previous study [7], the magnetic moments were initialized in the canted antiferromagnetic order with a canting angle of ≈67° magnitudes of ≈2 μ_B. The directions of the magnetic moments were constrained and spin-orbit coupling was activated. Again following [7], the Dudarev correction was set to U_{eff} = 3.4 eV. For this material, a time step of 0.5 fs was used for both the training and the production MD runs. Again, a linear temperature ramp was used for the training, with temperatures ranging from 1 K to 50 K. The total simulation length was 50000 time steps, which, together with the other MD parameters, implies a heating rate of ≈ 2 K/ps. Cutoff radii of 6 Å and 5 Å were used for the radial and angular descriptors, respectively. Production runs were carried out for a linear T-ramp from 1 K to 4 K, for which the results are not shown below, as well as constant temperatures of 1 K, 5 K, 15 K, 20 K, 25 K and 40 K. Similarly to the labeling of manganese ions in LMO, the osmium ions were labeled with indices ranging from 0 to 107. Again, PBE exchange-correlation potentials, the Langevin thermostat and the Parinello-Rahman algorithm were used.

Fig. 5.13 and 5.14 show a) the distribution of modes across the supercell, b) their site-site corraletions and c) the frequencies of specific values on heat maps for T = 1 K. Fig. 5.15 shows the same for the components of the rotation vector. The only temperature at which significant deviations from zero of Q_2 and Q_3 can be observed is T = 1 K. This is shown in Fig. 5.13 a) and c). At higher temperatures, these modes fluctuate around zero at each site. However, the magnitudes of Q_2 and Q_3 are not uniformly distributed across the supercell or exhibit cooperative phenomena, like in LMO. On the contrary, there exist some sites that exhibit large magnitudes of Q_2, or Q_3, while the average distortion at other sites is close to zero. The distortion

modes do not exhibit dynamic behavior on the time scale of the present simulations, as any given mode at any given site only thermally fluctuates around a constant average, which is zero in most cases. Additionally, a weak site-site correlation pattern is observed at T = 1 K, as shown in Fig. 5.13 b). According to this pattern, the Q_2 dynamics are positively correlated in plane and negatively correlated wrt. neighboring planes, which is the same pattern that was reported for the ground state structure in [7]. Again taking this as evidence for the existence of a critical temperature, this implies that the critical temperature is predicted to be at or below T_c = 1 K, which is lower than the ≈ 7 K reported by experiment [6, 51]. Q_4, Q_5 and Q_6 are not significantly different from zero at any temperature. Data for these modes is shown in Fig. 5.14.

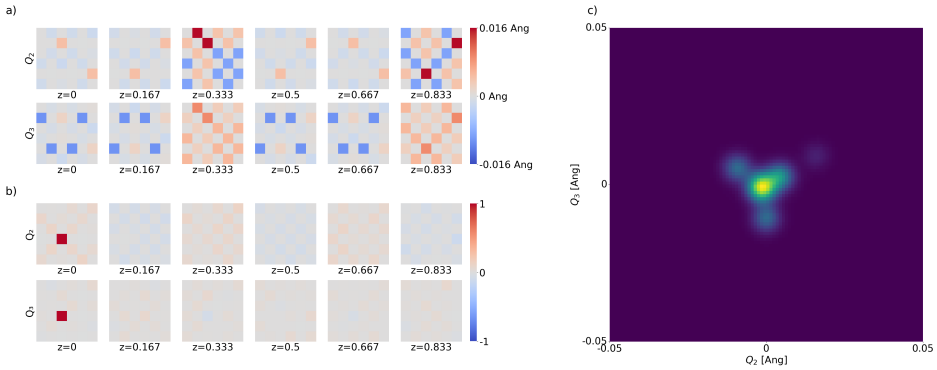

Figure 5.13: BNOO at $T = 1K$: a) averages of JT-modes Q_2 and Q_3 for each octahedron around an Os-site. b) Pearson correlation coefficients of JT-modes for each site wrt. site with index 12. c) Heat map of occurrences of JT distortion values across time and entire supercell. Brighter colors indicate a higher probability of an octahedron having a given distortion.

At low temperatures, the octahedra exhibit significant rotational modes that appear to be cooperative. The magnitude of these rotations is of the order of 8° and their dynamics appear to be correlated across the supercell. These findings are shown in Fig. 5.15 a) and b). There is a finite number of modes that the rotational axes occupy, and their pattern is shown in Fig. 5.15 c). The octahedral rotations appear to be static at low temperatures for a simulation length of 225 ps. At T ≈ 15 K, the octahedral rotation

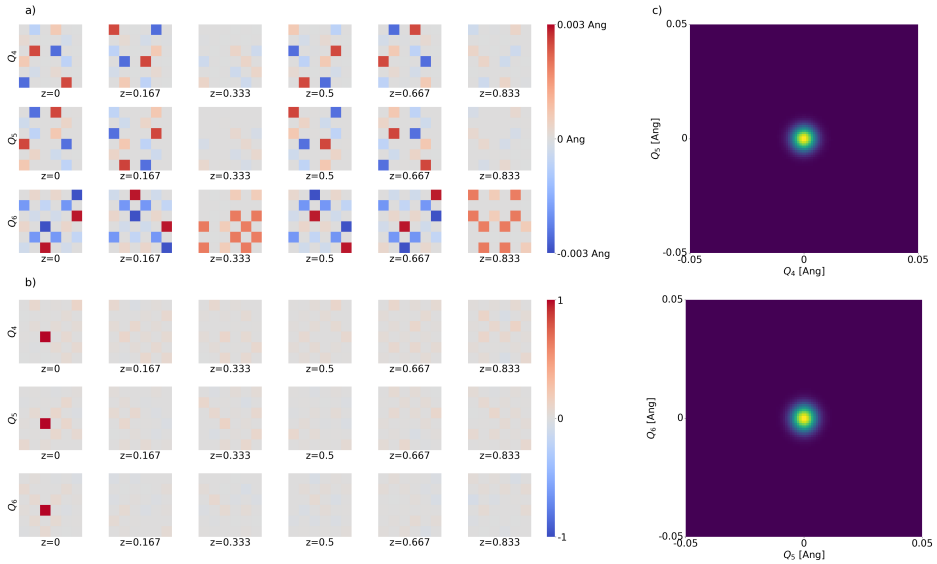

Figure 5.14: BNOO at $T = 1K$: a) averages of JT-modes Q_4, Q_5 and Q_6 for each octahedron around an Os-site. b) Pearson correlation coefficients of JT-modes for each site wrt. site with index 12. c) Heat map of occurrences of JT distortion values across time and entire supercell. Brighter colors indicate a higher probability of an octahedron having a given distortion.

axes begin to exhibit discontinuous "jumps" from one alignment to another. These "jumps" become more frequent with increasing temperature, as is shown in Fig. 5.16. At least close to T = 15 K, the entire supercell exhibits such transitions simultaneously. This is the behavior that one would expect for an adiabatic potential energy surface that has multiple local minima in the space of the coordinates of the rotational axes of all octahedra around osmium ions in the supercell. In this case, increasing temperature would introduce thermal transitions from one minimum to another, with a mean first passage time that decreases with increasing temperature.

An analysis of the dynamics of the Van Vleck modes and octahedral rotations shows significant fluctuations of the velocity-autocorrelation function of Q_2 and Q_3 up to a lag of around 5 ps, a shown in Fig. 5.17. These fluctuations persist up to high temperatures and their period appears independent of T and is of the order of 60-70 fs. Fig. 5.18 shows that the integrated velocity-autocorrelation time of these degrees of freedom decreases with temperature.

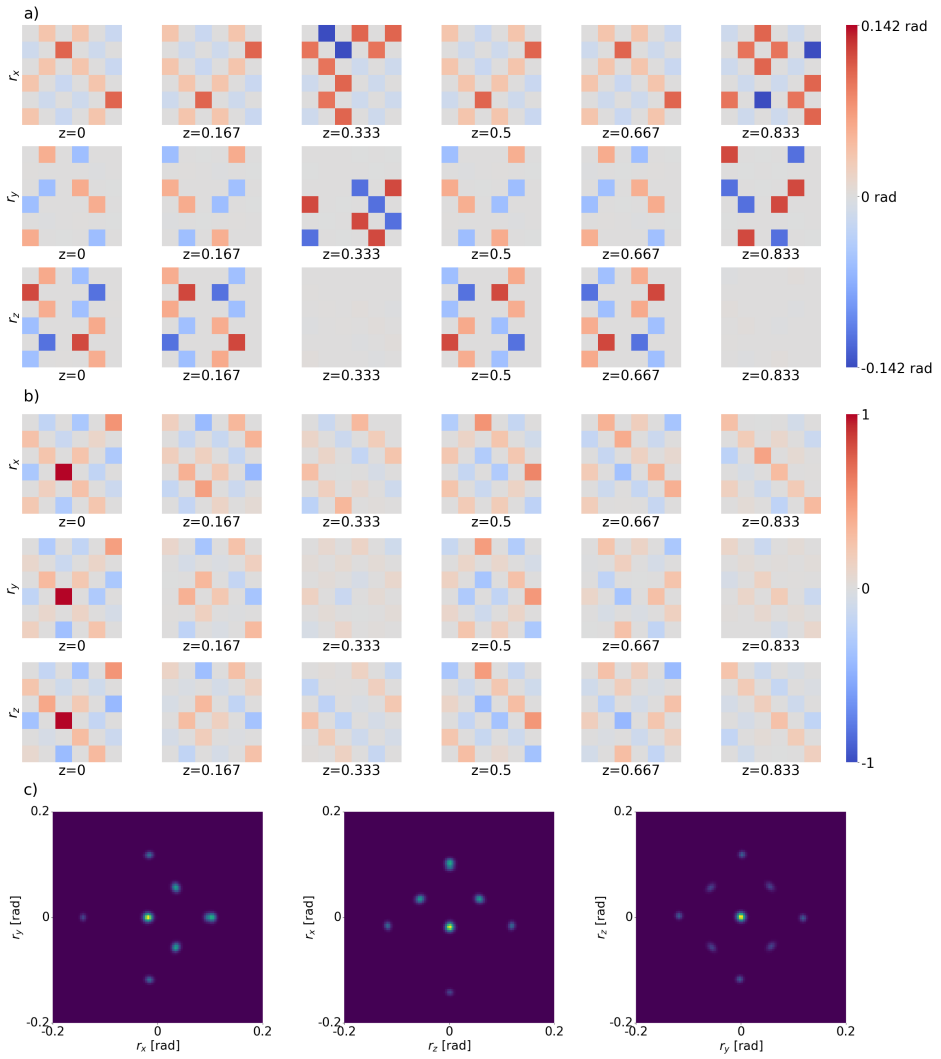

Figure 5.15: BNOO at $T = 1K$: a) averages of components of rotation vector for each octahedron around an Os-site. b) Pearson correlation coefficients of components of rotation vectors for each site wrt. site with index 12. c) Heat map of occurrences of rotation vector components across time and entire supercell. Brighter colors indicate a higher probability of an octahedron having a given rotation.

The dynamics of the degrees of freedom of barium atoms were also analyzed. Here, the corresponding velocity-autocorrelation function shows fluctuations with significantly larger period of around 300 ps that is again independent of temperature. This is shown in Fig. 5.19. The integrated velocity autocorrelation time of the barium degrees of freedom exhibits no significant

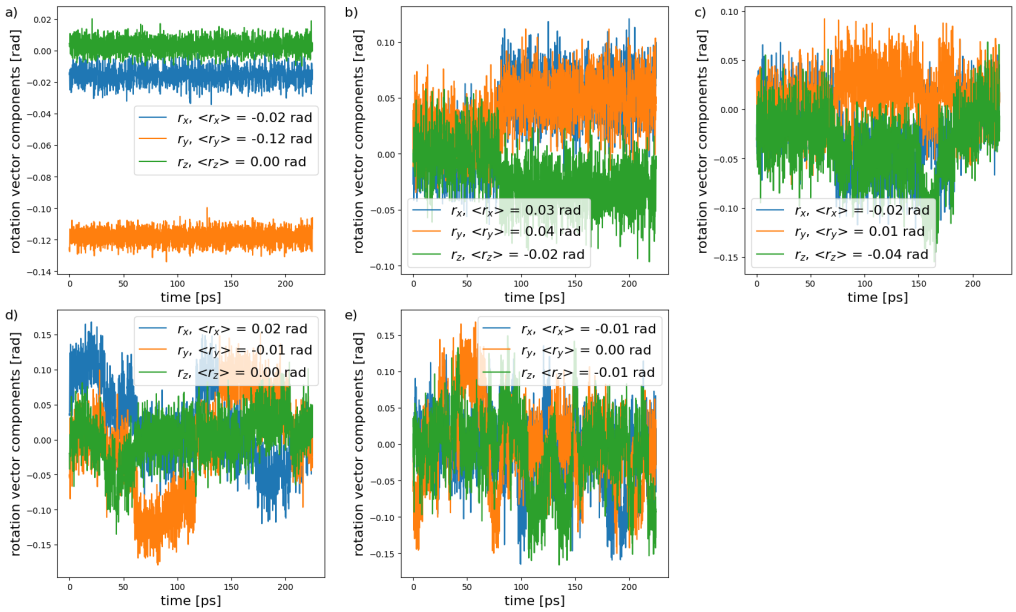

Figure 5.16: Time series for rotation vector components of octahedron with index 1 for T = a) 1K, b) 15K, c) 20K, d) 25K, e) 40K.

dependence on temperature, as can be seen from Fig. 5.20.

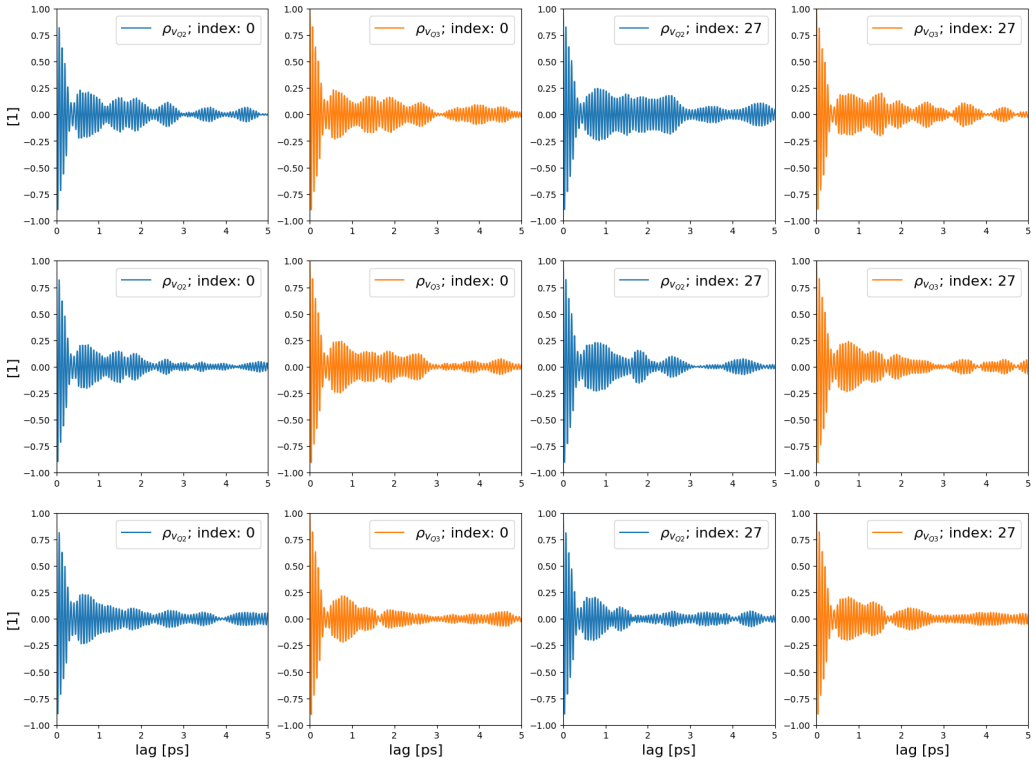

Figure 5.17: BNOO: Velocity-autocorrelation functions of Q2 and Q3 for indices 0 and 27 for: top row: T = 1K; middle row: T= 20K; bottom row: T = 40K. x-axis: t [ps]

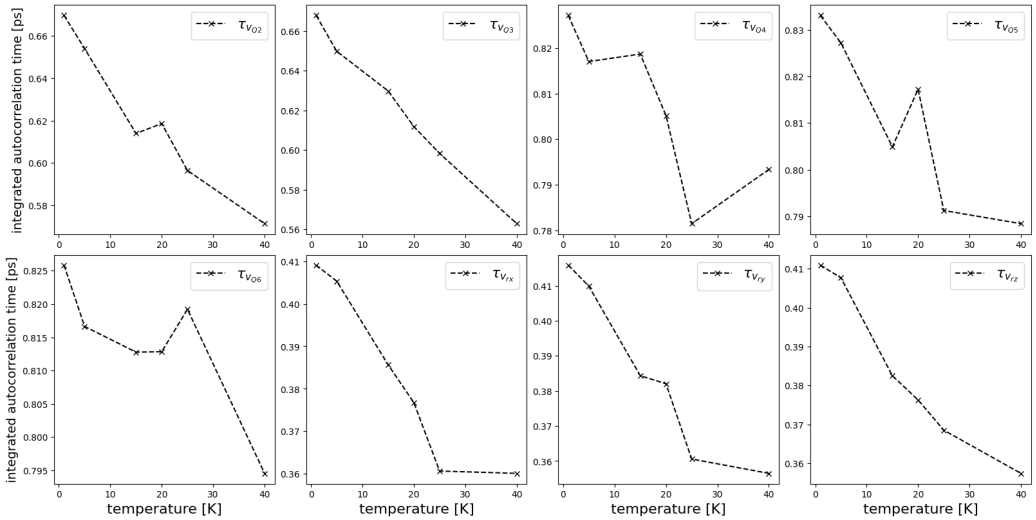

Figure 5.18: BNOO: Velocity-autocorrelation times of all Van Vleck modes and octahedral rotations as functions of temperature. The dashed lines are only guides for the eyes.

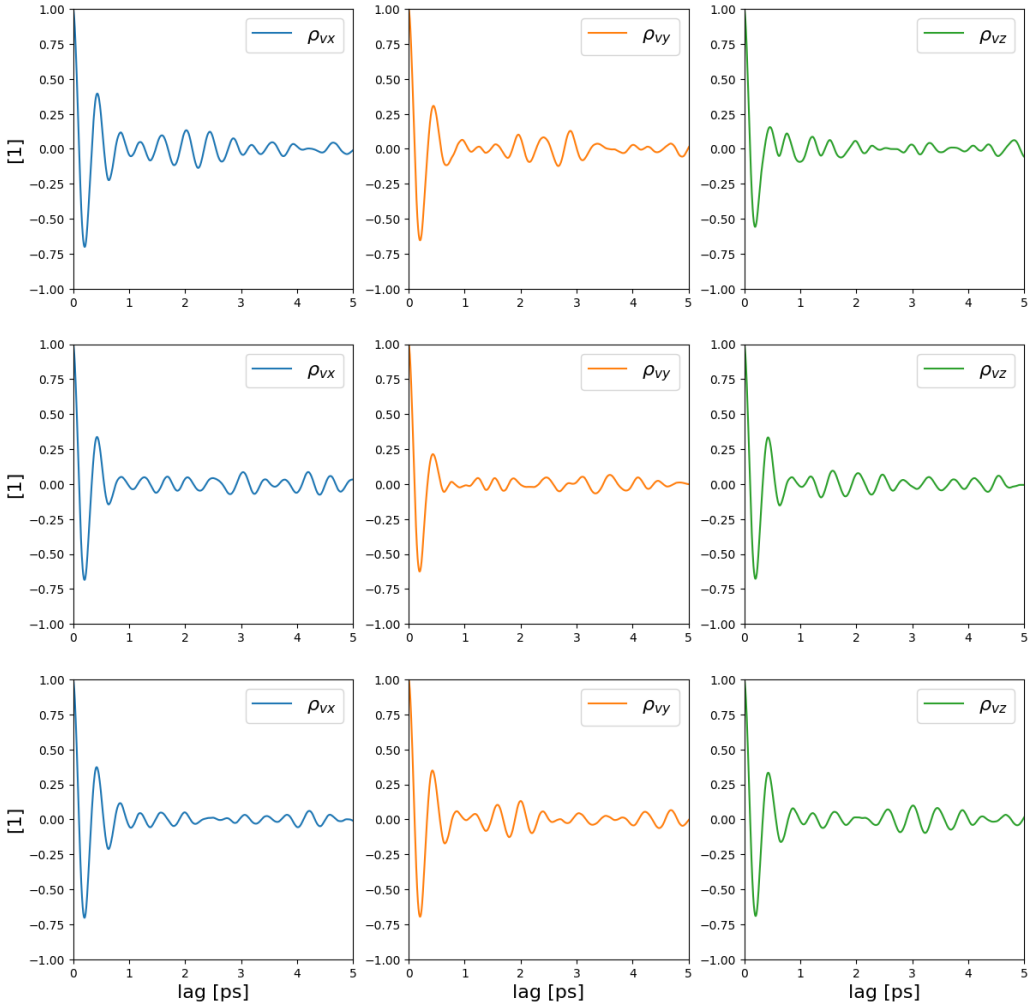

Figure 5.19: LMO: Velocity-autocorrelation functions of DOF of one Ba-ion for: top row: T = 1K; middle row: T= 20K; bottom row: T = 40K. x-axis: t [ps]

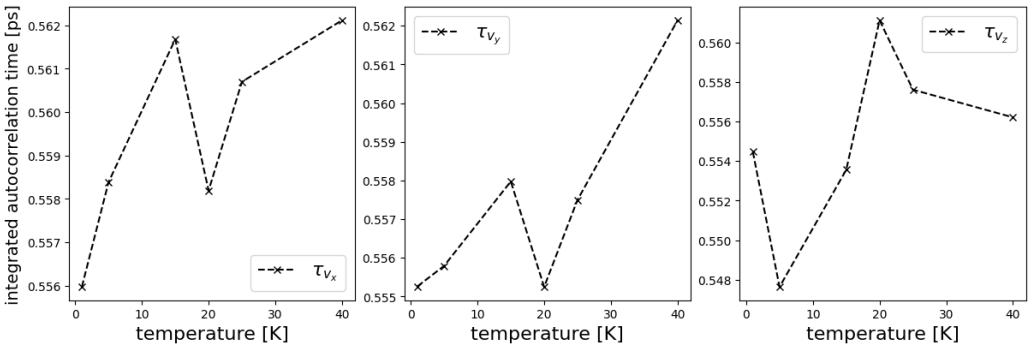

Figure 5.20: BNOO: Velocity-autocorrelation times of Ba DOF as functions of temperature. The dashed lines are only guides for the eyes.

Chapter 6

Conclusions

The results of the simulations with LMO are consistent with the results of the reference study [3] and build upon them. Most notably, the observation of an increased correlation length at the transition temperature is further evidence for an orbital ordering transition. Additionally, the cooperative behavior agrees with experimental results. However, some aspects of the experiment can not be reproduced with the methodolgy of this study. This includes the persistence of local JT-distorted clusters up to high temperatures. This could be due to the fact that the domains with the same structural distortion in the disordered phase are of similar size as the supercell that was used for the production runs and significantly larger than the supercell that was used for training [4]. It is therefore concluded that what has been simulated here is the order-to-disorder transition where only the Kugel-Khomskii superexchange is taken into account. The transition temperature is then in good agreement with theoretical predictions. Likewise, the shape of the potential energy surface that is implied by the heat maps in section 5.1 is in good agreement with theory and experiment [42]. Overall, these findings strengthen the evidence for the current understanding of structural and electronic phenomena in LMO.

The results for Q_4 to Q_6 disagree with the experiment [41] and it can not be definitively decided why they appear active in the reported results. To

the knowledge of the authors, there is no mention in the relevant literature of a pseudo JTE in LMO that would apply to the given situation and could be responsible for such distortions. Further research is proposed to learn more about the nature of these distortions. For example, it would be worthwhile to investigate whether these distortions lower the energy of the ground state. Additionally an analysis the electronic structure of a configuration with and without these distortions present would show whether it is plausible that they arise from electronic effects. However, methodological limitations can not be excluded. The choice of DFT-parameters, exchange-correlation functional or improved training of the MLFF could all significantly alter the results with respect to these distortion modes, especially because their magnitude is around four times smaller than that of Q_2 and Q_3.

With regard to the hypothesis mentioned in section 3 that the cooperative distortions in LMO are not due to the JTE but steric effects [49], this can not be excluded with certainty. The transition temperature of the octahedral rotations is the same as that of the Van Vleck modes. Furthermore, the value of U_{eff} also influences the magnitude of the rotations, not only the Van Vleck modes. It would therefore be expedient to investigate whether the presence of a transition of the Van Vleck modes depends on the presence od a rotational transition or vice versa or whether both transitions are independent. This could be done by machine learned molecular dynamics training and production runs with constrained octahedral rotations and constrained Van Vleck distortions, respectively, and could be a step towards a definitive conclusion on the matter.

To the knowledge of the authors, this study is the first time that the method of machine learned force fields was applied in conjunction with non-collinear magnetic moments and spin-orbit coupling. The physical properties of BNOO are strongly influenced by these phenomena and the material is therefore a good candidate to test the potential of the MLFF method with more complex DFT settings. Dynamic behavior of the Jahn-Teller distortions could not be reproduced and the transition temperature implied by the long range correlation of Q_2 at T = 1 K is significantly lower than any of the ex-

perimentally reported transition temperatures [51]. This could be due to the fact that the adiabatic approximation does not capture quantum mechanic behavior of the lattice. However, the existence of long range correlations with the same pattern as the staggered JT-distortions of the ground state [7] leave open the possibility that molecular dynamics simulations at even lower temperatures will show cooperative distortions similar to the ground state. Another important aspect is the fact that the JT-distortions reported from experiment and computations are much smaller than those of for example LMO. Since they are also very sensitive with respect to electronic or magnetic structure (for example the canting angle of the magnetic moments [7]), it is possible that careful tweaking of the DFT parameters and the MLFF training could improve on the present results. The limits of the capabilities of the present machine learning method are, however, not clear. One limitation is the fact that the MLFF cannot learn magnetic information directly. Only if magnetic effects influence the lattice configuration, magnetism can be learned indirectly from structural information. However, the phase transition of BNOO below which order is established is both magnetic and structural [51].

The fact that there are individual sites with stronger distortions might come from the formation of polarons, quasiparticles that emerge from the self-trapping of charge carriers due to structural distortions. The possibility of polaron formation has been attested in the literature [58, 59]. Further research is required to test the validity of this hypothesis.

The significant octahedral rotations and their dynamic behaviour are another phenomenon that has not been reported before. It should carefully be examined whether they can be reproduced and if that is the case their nature should be investigated. It is not clear how they contribute to the formation of the broken local point symmetry phase, but the lowest temperature at which the "jumps" of the rotational axes occur is in the range of the BLPS transition temperature. Octahedral rotations have not been found to be necessary for the formation of this phase, but they have also not been excluded definitively, as described in section 4. The BLPS transition is re-

ported to be a real phase transition [6], so if the octahedral rotations play a role in the formation of this phase, it is not clear what the order parameter is.

All in all it can be concluded that the method that yields results that are in good agreement with the experiment for LMO and orbital ordering cannot be applied to the more complex situation of non-collinear magnetic moments and spin orbit coupling in BNOO. Tweaking of the parameters and the machine learning process could improve results, but it is not clear whether traces of the dynamic JTE can be reproduced with this method, which applies the adiabatic approximation.

Appendix A: Formulae

The analysis of the results of this study was done using the python packages numpy and scipy [60, 61]. The formulae below are described the way that they are implemented in these packages.

Site-site correlations are calculated using the Pearson correlation coefficient [62]

$$r_{xy} = \frac{\sum_i (x_i - \bar{x})(y_i - \bar{y})}{\sqrt{\sum_i (x_i - \bar{x})^2}\sqrt{\sum_i (y_i - \bar{y})^2}}. \tag{6.1}$$

The estimator used for autocorrelation functions is

$$\rho_A(t) = \frac{\frac{1}{T-t-1}\sum_{\tau=0}^{T-t-1} A_{\tau+t} * A_\tau \; - \; \left(\frac{1}{T-t-1}\sum_{\tau=0}^{T-t-1} A_\tau\right)\left(\frac{1}{T-t-1}\sum_{\tau=0}^{T-t-1} A_{\tau+t}\right)}{\tilde{\sigma}_A^2}, \tag{6.2}$$

where T is the length of the signal and

$$\tilde{\sigma}_A^2 = \overline{A^2} - \overline{A}^2 \tag{6.3}$$

is an estimator for the variance of A with the overline denoting a time average of a quantity.

Fourier transforms are calculated as follows:

$$\tilde{A}_f = \frac{1}{\sqrt{T}} \sum_{t=0}^{T-1} A_t \exp\left\{-2\pi i \frac{tf}{T}\right\}. \tag{6.4}$$

The power spectrum of a signal A_t is defined as the square of the absolute value of its Fourier transform: $|\tilde{A}_f|^2$.

To calculate an integrated autocorrelation time, the envelope of the corresponding autocorrelation is computed first:

$$env\left[\rho_A\right](t) = \mathcal{F}^{-1}[\mathcal{F}[\rho_A(t)]2U] = \rho_A(t) + i\mathcal{H}\{\rho_A\}(t), \tag{6.5}$$

where $\mathcal{F}$ denotes the Fourier transform, $\mathcal{H}$ denotes the Hilbert transform, and U the unit step function. Then, the integrated autocorrelation time is calculated with this formula:

$$\tau_{A,int} = t_0 * \left[\frac{1}{2} + \sum_{t=1}^{T^*} env\left[\rho_A\right](t)(1 - t/T)\right], \tag{6.6}$$

where t_0 is the duration between two reported configurations, T is the total length of the signal and $T*$ is some number chosen to be significantly larger than $\tau_{A,int}$ but possibly less than T. The velocity-autocorrelation times that are reported are averaged over the entire supercell.

Appendix B: Octahedral rotations with the VanVleckCalculator

The package VanVleckCalculator [56, 57] provides an algorithm that iteratively rotates octahedra to orient them in a way that their axes most optimally align with the crystallographic axes of the high-symmetry reference structure. However, there is no way to output the total rotation in the form of a rotational axis and an angle. The rotations are therefore calculated this way:

Let $\mathbf{a}, \mathbf{b}, \mathbf{c}$ be the vectors of the original octahedral axes, and $\mathbf{a'}, \mathbf{b'}, \mathbf{c'}$ the vectors of the octahedral axes after it has been automatically rotated by VanVleckCalculator. The second set of vectors should be close to the crystallographic basis. We can then implicitly define rotation matrices

$$(\mathbf{a}, \mathbf{b}, \mathbf{c}) = R^1 (\mathbf{e_x}, \mathbf{e_y}, \mathbf{e_z}) , \tag{6.7}$$

$$(\mathbf{a'}, \mathbf{b'}, \mathbf{c'}) = R^2 (\mathbf{e_x}, \mathbf{e_y}, \mathbf{e_z}) . \tag{6.8}$$

The total rotation is then described by rotation matrix R:

$$\begin{aligned} (\mathbf{a}, \mathbf{b}, \mathbf{c}) &= R (\mathbf{a'}, \mathbf{b'}, \mathbf{c'}) \\ &= R^1 R^{2^{-1}} (\mathbf{a'}, \mathbf{b'}, \mathbf{c'}) \\ &= R^1 R^{2^T} (\mathbf{a'}, \mathbf{b'}, \mathbf{c'}) \\ &= \left[(\mathbf{a}, \mathbf{b}, \mathbf{c}) (\mathbf{a'}, \mathbf{b'}, \mathbf{c'})^T \right] (\mathbf{a'}, \mathbf{b'}, \mathbf{c'}) , \end{aligned} \tag{6.9}$$

which can be written w.r.t the crystallographic basis $\{\mathbf{e_i}\}$ as

$$[R]_{\{\mathbf{e_i}\}} = \begin{pmatrix} a_x a'_x + b_x b'_x + c_x c'_x & a_x a'_y + b_x b'_y + c_x c'_y & a_x a'_z + b_x b'_z + c_x c'_z \\ a_y a'_x + b_y b'_x + c_y c'_x & a_y a'_y + b_y b'_y + c_y c'_y & a_y a'_z + b_y b'_z + c_y c'_z \\ a_z a'_x + b_z b'_x + c_z c'_x & a_z a'_y + b_z b'_y + c_z c'_y & a_z a'_z + b_z b'_z + c_z c'_z \end{pmatrix}, \tag{6.10}$$

where $a_i, b_i, c_i, a'_i, b'_i, c'_i$ are the components of the vectors $\mathbf{a}, \mathbf{b}, \mathbf{c}, \mathbf{a'}, \mathbf{b'}, \mathbf{c'}$ w.r.t. the basis $\{\mathbf{e_i}\}$.

The rotation angle θ is then given by

$$|\theta| = \arccos\left(\frac{\mathrm{Tr}[R] - 1}{2}\right), \tag{6.11}$$

and (under the assumption that $\theta \neq 0$ and $\theta \neq \pi$) the unit vector of the rotational axis $\hat{n}$ is given by

$$[\hat{n}]_{\{\mathbf{e_i}\}} = \frac{\begin{pmatrix} a_z a'_y + b_z b'_y + c_z c'_y - a_y a'_z + b_y b'_z + c_y c'_z \\ a_x a'_z + b_x b'_z + c_x c'_z - a_z a'_x + b_z b'_x + c_z c'_x \\ a_y a'_x + b_y b'_x + c_y c'_x - a_x a'_y + b_x b'_y + c_x c'_y \end{pmatrix}}{\left|\left| \begin{pmatrix} a_z a'_y + b_z b'_y + c_z c'_y - a_y a'_z + b_y b'_z + c_y c'_z \\ a_x a'_z + b_x b'_z + c_x c'_z - a_z a'_x + b_z b'_x + c_z c'_x \\ a_y a'_x + b_y b'_x + c_y c'_x - a_x a'_y + b_x b'_y + c_x c'_y \end{pmatrix} \right|\right|}. \tag{6.12}$$

The "rotation vector" $\mathbf{r}$ that is shown in the plots is defined such that it has the rotation angle in radians as magnitude and the direction of the rotation axis in such way that the rotation is counterclockwise wrt. the "rotation vector".

Appendix C: LMO sample INCAR

Reference for this sample INCAR file and for the training with LMO in general was taken from [3].

#General System = LMO
ISTART = 0 #continue = 1, from scratch = 0
ICHARG = 2 #continue = 1, superpostion of atomic charge densities = 2
ENCUT = 500
ISMEAR = 0
SIGMA = 0.05
NEDOS = 901
NCORE = 4
KPAR = 4

#magnetism
ISPIN = 2
MAGMOM = 8*0 4 4 4 4 -4 -4 -4 -4 24*0

#U
LORBIT = 11
LDAU = .TRUE.
LDAUTYPE = 2
LDAUL = -1 2 -1 #l quantum number to which U is added. -1 no, l = 2 d orbirtal

LDAUU = 0 3.5 0 #U which is added to every atom, so U = 3.5 for Mn d orbital
LDAUJ = 0 0.0 0
LMAXMIX = 4

#MD
ISYM = 0
ISIF = 3
MDALGO=3 #use Langevin thermostat
LANGEVIN_GAMMA = 1.0 1.0 1.0 #friction coef. for atomic DoFs for each species (A B X_3)
LANGEVIN_GAMMA_L=3.0 #friction coef. for the lattice DoFs
PMASS=300 #mass for lattice DoFs
LATTICE_CONSTRAINTS = T T T
PSTRESS=0.001 #P is set at 0.001 KB.
POTIM = 0.5 #MD timestep in fs
IBRION = 0
SMASS = 0
TEBEG = 600 #start temp
TEEND = 650 #end temp
NSW = 12500 #8 K/ps
NBLOCK = 1
NWRITE = 1
NELM = 100
INIWAV = 1
IWAVPR = 1
LWAVE = .FALSE.
LCHARG = .FALSE.

#MACHINE-LEARNING
ML_MCONF = 2000
ML_LMLFF = .TRUE. # Set as LMLFF_FF = .TRUE., when some machine-learning force field calculations are executed. Default is .FALSE.
ML_ISTART = 0 # Parameter to control restarting calculations. Set 0, 1 or

2. When you execute the training from the scratch, this needs to be set to 0. When you restart the training reading the previous ab initio data (ABCAR file), this needs to be set to 1. When you only want to use the force field and no DFT this has to be 2.
ML_RCUT1 = 6.0 # Cutoff radius used for calculating the radial descriptor. Default is RCUT2_FFM.
ML_RCUT2 = 5.0 # Cutoff radius used for calculating the angular descriptor. Default is 5.0 (Angst).

Appendix D: BNOO sample INCAR

#optimisation
SYSTEM=BNOO
NCORE = 8
KPAR = 4

#dos
ISMEAR = 0
SIGMA = 0.008
ISYM = -1
KSPACING = 0.16

#electronic minimisation
ISTART = 0
ENCUT = 600
PREC = Accurate
LREAL = A
LMAXMIX = 4

#magnetism
LSORBIT = T
MAGMOM = 12*0.0 -0.7492 1.8544 0.0000 1.8544 -0.7492 0.0000 -0.7492 1.8544 0.0000 1.8544 -0.7492 0.0000 96*0.0
I_CONSTRAINED_M = 1

RWIGS = 1.164 1.413 1.979 0.820
LAMBDA = 10
M_CONSTR = 12*0.0 -0.7492 1.8544 0.0000 1.8544 -0.7492 0.0000 -0.7492 1.8544 0.0000 1.8544 -0.7492 0.0000 96*0.0

#mixing
AMIX = 0.3
BMIX = 0.0001
AMIX_MAG = 0.4
BMIX_MAG = 0.0001

#Dudarev
LDAU = T
LDAUTYPE = 2
LDAUL = -1 2 -1 -1
LDAUU = 0.0 3.4 0.0 0.0
LDAUJ = 0.0 0.0 0.0 0.0
LDAUPRINT = 2

#MD
ISIF = 3
MDALGO = 3
LANGEVIN_GAMMA = 1.0 1.0 1.0 1.0
LANGEVIN_GAMMA_L = 3.0
PMASS = 300
LATTICE_CONSTRAINTS = T T T
PSTRESS = 0.001
POTIM = 0.5
IBRION = 0
SMASS = 0
TEBEG = 1
TEEND = 10
NSW = 10000
NBLOCK = 1
NWRITE = 1

NELM = 100
INIWAV = 1
IWAVPR = 1

# machine learning
ML_MCONF = 2000
ML_LMLFF = .TRUE.
ML_MODE = train
ML_RCUT1 = 6.0 #Cutoff radius used for calculating the radial descriptor. Default is RCUT2_FFM.
ML_RCUT2 = 5.0 #Cutoff radius used for calculating the angular descriptor. Default is 5.0 (Angst).

#output
LORBMOM = T
LORBIT = 11
LWAVE = F
LCHARG = F

Bibliography

[1] Ryosuke Jinnouchi et al. "Phase Transitions of Hybrid Perovskites Simulated by Machine-Learning Force Fields Trained on the Fly with Bayesian Inference". In: *Phys. Rev. Lett.* 122 (22 June 2019), p. 225701. DOI: 10.1103/PhysRevLett.122.225701.

[2] Ryosuke Jinnouchi, Ferenc Karsai, and Georg Kresse. "On-the-fly machine learning force field generation: Application to melting points". In: *Phys. Rev. B* 100 (1 July 2019), p. 014105. DOI: 10.1103/PhysRevB.100.014105.

[3] Thies Jansen, Geert Brocks, and Menno Bokdam. "Phase transitions of $LaMnO_3$ and $SrRuO_3$ from DFT + U based machine learning force fields simulations". In: *Phys. Rev. B* 108 (23 Dec. 2023), p. 235122. DOI: 10.1103/PhysRevB.108.235122.

[4] Xiangyun Qiu et al. "Orbital Correlations in the Pseudocubic O and Rhombohedral R Phases of $LaMnO_3$". In: *Phys. Rev. Lett.* 94 (17 May 2005), p. 177203. DOI: 10.1103/PhysRevLett.94.177203.

[5] J. Rodríguez-Carvajal et al. "Neutron-diffraction study of the Jahn-Teller transition in stoichiometric $LaMnO_3$". In: *Phys. Rev. B* 57 (6 Feb. 1998), R3189–R3192. DOI: 10.1103/PhysRevB.57.R3189.

[6] Kristin Willa et al. "Phase transition preceding magnetic long-range order in the double perovskite Ba_2NaOsO_6". In: *Phys. Rev. B* 100 (4 July 2019), p. 041108. DOI: 10.1103/PhysRevB.100.041108.

[7] Dario Fiore Mosca et al. "Interplay between multipolar spin interactions, Jahn-Teller effect, and electronic correlation in a $J_{\text{eff}} = \frac{3}{2}$ insula-

tor". In: *Phys. Rev. B* 103 (10 Mar. 2021), p. 104401. DOI: 10.1103/PhysRevB.103.104401.

[8] N. Iwahara. "Dynamic Jahn–Teller Phenomena in Heavy Transition Metal Compounds". In: *Journal of the Physical Society of Japan* 93.12 (2024), p. 121003. DOI: 10.7566/JPSJ.93.121003.

[9] H. A. Jahn and E. Teller. "Stability of polyatomic molecules in degenerate electronic states. I. Orbital degeneracy". In: *Proceedings of the Royal Society of London Series A* 161 (905 1937), pp. 220–235. DOI: 10.1098/rspa.1937.0142.

[10] D. I. Khomskii. *Transition Metal Compounds*. Cambridge: Cambridge University Press, 2014.

[11] L. Lu et al. "Magnetism and local symmetry breaking in a Mott insulator with strong spin orbit interactions". In: *Nature Communications* 8 (1 2017), p. 14407. DOI: 10.1038/ncomms14407. URL: https://doi.org/10.1038/ncomms14407.

[12] A. S. Erickson et al. "Ferromagnetism in the Mott Insulator Ba_2NaOsO_6". In: *Phys. Rev. Lett.* 99 (1 July 2007), p. 016404. DOI: 10.1103/PhysRevLett.99.016404.

[13] Naoya Iwahara, Veacheslav Vieru, and Liviu F. Chibotaru. "Spin-orbital-lattice entangled states in cubic d^1 double perovskites". In: *Phys. Rev. B* 98 (7 Aug. 2018), p. 075138. DOI: 10.1103/PhysRevB.98.075138.

[14] I. B. Bersuker. *The Jahn-Teller Effect*. Cambridge: Cambridge University Press, 2006.

[15] B. Brandsen and C. Joachain. *Physics of atoms and molecules*. Harlow: Longman Group UK Limited, 1983.

[16] T. Azumi and K. Matsuzaki. "What does the term "vibronic coupling" mean?" In: *Photochemistry and Photobiology* 25 (3 1977), pp. 315–326. DOI: 10.1111/j.1751-1097.1977.tb06918.x.

[17] R. Heid. "Electron-Phonon Coupling". In: *The Physics of Correlated Insulators, Metals, and Superconductors*. Ed. by E. Pavarini et al. Vol. 7. Jülich: Forschungszentrum Jülich GmbH, Institute for Advanced Simulation, 2017. Chap. 15.

[18] I. B. Bersuker. "Pseudo-Jahn–Teller Effect—A Two-State Paradigm in Formation, Deformation, and Transformation of Molecular Systems

and Solids". In: *Chem. Rev.* 113 (3 2013), pp. 1351–1390. DOI: 10.1021/cr300279n.

[19] C. F. Schwenk and B. M. Rode. "New insights into the Jahn-Teller effect through ab initio quantum-mechanical/molecular-mechanical molecular dynamics simulations of CuII in water." In: *Chemphyschem* 4.9 (Sept. 2003), pp. 931–43. DOI: 10.1002/cphc.200300659.

[20] Joseph C. A. Prentice, Bartomeu Monserrat, and R. J. Needs. "First-principles study of the dynamic Jahn-Teller distortion of the neutral vacancy in diamond". In: *Phys. Rev. B* 95 (1 Jan. 2017), p. 014108. DOI: 10.1103/PhysRevB.95.014108.

[21] G. Kresse and J. Hafner. "Ab initio molecular dynamics for liquid metals". In: *Phys. Rev. B* 47 (1 Jan. 1993), pp. 558–561. DOI: 10.1103/PhysRevB.47.558.

[22] G. Kresse and J. Furthmüller. "Efficiency of ab-initio total energy calculations for metals and semiconductors using a plane-wave basis set". In: *Computational Materials Science* 6.1 (1996), pp. 15–50. ISSN: 0927-0256. DOI: https://doi.org/10.1016/0927-0256(96)00008-0.

[23] G. Kresse and J. Furthmüller. "Efficient iterative schemes for ab initio total-energy calculations using a plane-wave basis set". In: *Phys. Rev. B* 54 (16 Oct. 1996), pp. 11169–11186. DOI: 10.1103/PhysRevB.54.11169.

[24] G. Kresse and D. Joubert. "From ultrasoft pseudopotentials to the projector augmented-wave method". In: *Phys. Rev. B* 59 (3 Jan. 1999), pp. 1758–1775. DOI: 10.1103/PhysRevB.59.1758.

[25] R. G. Parr and W. Yang. *Density-Functional Theory of Atoms and Molecules*. New York: Oxford University Press, 1994.

[26] L. H. Thomas. "The calculation of atomic fields". In: *Mathematical Proceedings of the Cambridge Philosophical Society* 23 (1927), pp. 542–548.

[27] E. Fermi. "Eine statistische Methode zur Bestimmung einiger Eigenschaften des Atoms und ihre Anwendung auf die Theorie des periodischen Systems der Elemente". In: *Zeitschrift für Physik* 48 (1928), pp. 73–79.

[28] P. Hohenberg and W. Kohn. “Inhomogenous Electron Gas”. In: *Physical Review* 136 (1964), B864–B871.

[29] W. Kohn and L. J. Sham. “Self-Consistent Equations Including Exchange and Correlation Effects”. In: *Physical Review* 140 (1965), A1133–A1138.

[30] J. F. Janak. “Proof that $\frac{\partial E}{\partial n_i} = \epsilon_i$ in density-functional theory”. In: *Physical Review B* 18 (1978), pp. 7165–7168.

[31] John P. Perdew, Kieron Burke, and Matthias Ernzerhof. “Generalized Gradient Approximation Made Simple”. In: *Phys. Rev. Lett.* 77 (18 Oct. 1996), pp. 3865–3868. DOI: 10.1103/PhysRevLett.77.3865.

[32] F. Giustino. *Materials Modelling using Density Functional Theory: Properties and Predictions*. Oxford: Oxford University Press, 2014.

[33] *The VASP Manual - VASP Wiki*. https://vasp.at/wiki/The_VASP_Manual. Accessed: 2025-09-29.

[34] S. L. Dudarev et al. “Electron-energy-loss spectra and the structural stability of nickel oxide: An LSDA+U study”. In: *Phys. Rev. B* 57 (3 Jan. 1998), pp. 1505–1509. DOI: 10.1103/PhysRevB.57.1505.

[35] Vladimir I. Anisimov, Jan Zaanen, and Ole K. Andersen. “Band theory and Mott insulators: Hubbard U instead of Stoner I”. In: *Phys. Rev. B* 44 (3 July 1991), pp. 943–954. DOI: 10.1103/PhysRevB.44.943.

[36] W. C. Swope et al. “A computer simulation method for the calculation of equilibrium constants for the formation of physical clusters of molecules: Application to small water clusters.” In: *J. Chem. Phys.* 76 (1 Jan. 1982), pp. 637–649. DOI: 10.1063/1.442716.

[37] M. Tuckerman, B. J. Berne, and G. J. Martyna. “Reversible multiple time scale molecular dynamics”. In: *The Journal of Chemical Physics* 97.3 (Aug. 1992), pp. 1990–2001. ISSN: 0021-9606. DOI: 10.1063/1.463137.

[38] H. F. Trotter. “On the Product of Semi-Groups of Operators.” In: *Proceedings of the American Mathematical Society* 10.4 (Sept. 1959), pp. 545–551. DOI: 10.2307/2033649.

[39] Ernst Hairer, Christian Lubich, and Gerhard Wanner. “Geometric numerical integration illustrated by the Störmer–Verlet method”. In: *Acta Numerica* 12 (2003), pp. 399–450. DOI: 10.1017/S0962492902000144.

[40] M. Parrinello and A. Rahman. "Crystal Structure and Pair Potentials: A Molecular-Dynamics Study". In: *Phys. Rev. Lett.* 45 (14 Oct. 1980), pp. 1196–1199. DOI: 10.1103/PhysRevLett.45.1196.

[41] P. Norby et al. "The crystal structure of lanthanum manganate(iii), LaMnO3, at room temperature and at 1273 K under N2". In: *Journal of Solid State Chemistry* 119.1 (1995), pp. 191–196. ISSN: 0022-4596. DOI: https://doi.org/10.1016/0022-4596(95)80028-N.

[42] Eva Pavarini and Erik Koch. "Origin of Jahn-Teller Distortion and Orbital Order in $LaMnO_3$". In: *Phys. Rev. Lett.* 104 (8 Feb. 2010), p. 086402. DOI: 10.1103/PhysRevLett.104.086402.

[43] E. O. Wollan and W. C. Koehler. "Neutron Diffraction Study of the Magnetic Properties of the Series of Perovskite-Type Compounds $[(1-x)\mathrm{La}, x\mathrm{Ca}]\mathrm{MnO}_3$". In: *Phys. Rev.* 100 (2 Oct. 1955), pp. 545–563. DOI: 10.1103/PhysRev.100.545.

[44] Tao Geng, Zengzhi Han, and Songlin Zhuang. "Effective Coulomb interaction in LaMnO3". In: *Physica B: Condensed Matter* 405.17 (2010), pp. 3714–3716. ISSN: 0921-4526. DOI: https://doi.org/10.1016/j.physb.2010.05.072.

[45] Wei-Guo Yin, Dmitri Volja, and Wei Ku. "Orbital Ordering in $LaMnO_3$: Electron-Electron versus Electron-Lattice Interactions". In: *Phys. Rev. Lett.* 96 (11 Mar. 2006), p. 116405. DOI: 10.1103/PhysRevLett.96.116405.

[46] W. Y. Hu et al. "Jahn-Teller effect and many-body correlation effect in $LaMnO_3$". In: *Phys. Rev. B* 61 (2 Jan. 2000), pp. 1223–1231. DOI: 10.1103/PhysRevB.61.1223.

[47] H. Sawada et al. "Jahn-Teller distortion and magnetic structures in LaMnO3". In: *Journal of Magnetism and Magnetic Materials* 177-181 (1998). International Conference on Magnetism (Part II), pp. 879–880. ISSN: 0304-8853. DOI: https://doi.org/10.1016/S0304-8853(97)00451-4.

[48] Pablo Rivero, Vincent Meunier, and William Shelton. "Electronic, structural, and magnetic properties of $LaMnO_3$ phase transition at high temperature". In: *Phys. Rev. B* 93 (2 Jan. 2016), p. 024111. DOI: 10.1103/PhysRevB.93.024111.

[49] Julien Varignon, Manuel Bibes, and Alex Zunger. "Origins versus fingerprints of the Jahn-Teller effect in d-electron ABX_3 perovskites". In: *Phys. Rev. Res.* 1 (3 Nov. 2019), p. 033131. DOI: 10.1103/PhysRevResearch.1.033131.

[50] Jagadesh Kopula Kesavan et al. "Doping Evolution of the Local Electronic and Structural Properties of the Double Perovskite Ba2Na1–xCaxOsO6". In: *The Journal of Physical Chemistry C* 124.30 (2020), pp. 16577–16585. DOI: 10.1021/acs.jpcc.0c04807.

[51] W. Liu et al. "Phase diagram of Ba 2 NaOsO 6, a Mott insulator with strong spin orbit interactions". In: *Physica B: Condensed Matter* 536 (2018), pp. 863–866. ISSN: 0921-4526. DOI: https://doi.org/10.1016/j.physb.2017.08.062.

[52] Rong Cong et al. "First principles calculations of the electric field gradient tensors of Ba2NaOsO6, a Mott insulator with strong spin orbit coupling". In: *Journal of Physics: Condensed Matter* 32.40 (July 2020), p. 405802. DOI: 10.1088/1361-648X/ab9056. URL: https://doi.org/10.1088/1361-648X/ab9056.

[53] W. Liu et al. "Nature of lattice distortions in the cubic double perovskite Ba_2NaOsO_6". In: *Phys. Rev. B* 97 (22 June 2018), p. 224103. DOI: 10.1103/PhysRevB.97.224103.

[54] R. Cong et al. "Evidence from first-principles calculations for orbital ordering in Ba_2NaOsO_6: A Mott insulator with strong spin-orbit coupling". In: *Phys. Rev. B* 100 (24 Dec. 2019), p. 245141. DOI: 10.1103/PhysRevB.100.245141.

[55] J. H. Van Vleck. "The Jahn-Teller Effect and Crystalline Stark Splitting for Clusters of the Form XY6". In: *The Journal of Chemical Physics* 7.1 (Jan. 1939), pp. 72–84. DOI: 10.1063/1.1750327.

[56] Liam. A. V. Nagle-Cocco and Siân E. Dutton. "Van Vleck analysis of angularly distorted octahedra using *VanVleckCalculator*". In: *Journal of Applied Crystallography* 57.1 (Feb. 2024), pp. 20–33. DOI: 10.1107/S1600576723009925.

[57] Liam. A. V. Nagle-Cocco. *GitHub - lnaglecocco/VanVleckCalculator*. https://github.com/lnaglecocco/VanVleckCalculator. Accessed: 2025-10-11.

[58] L. Celiberti. "Small polarons in Spin-Orbit coupled osmates". Available at `https://amslaurea.unibo.it/id/eprint/24839/1/main.pdf`. Master's thesis. University of Bologna.

[59] L. Celiberti, D. Fiore Mosca, and G. et al. Allodi. "Spin-orbital Jahn-Teller bipolarons". In: *Nature Communications* 15 (1 Mar. 2024), p. 2429. DOI: `10.1038/s41467-024-46621-0`.

[60] *NumPy Documentation*. `https://numpy.org/doc/`. Accessed: 2025-10-11.

[61] *SciPy v1.16.2 Manual*. `https://docs.scipy.org/doc/scipy/`. Accessed: 2025-10-11.

[62] Karl Pearson. "Note on Regression and Inheritance in the Case of Two Parents". In: *Proceedings of the Royal Society of London* 58 (1895), pp. 240–242. URL: `https://www.jstor.org/stable/115794`.